A Search for Direct CP Violation in Two-Body Cabibbo-Suppressed Decays of Neutral Charmed Mesons

Christian Julienne Flacco

SLAC-R-886

Prepared for the Department of Energy
under contract number DE-AC02-76SF00515

Printed in the United States of America. Available from the National Technical Information Service, U.S. Department of Commerce, 5285 Port Royal Road, Springfield, VA 22161.

UNIVERSITY OF CALIFORNIA
SANTA CRUZ

A SEARCH FOR DIRECT *CP* VIOLATION IN TWO-BODY CABIBBO-SUPPRESSED DECAYS OF NEUTRAL CHARMED MESONS

A dissertation submitted in partial satisfaction of
the requirements for the degree of

DOCTOR OF PHILOSOPHY

in

PHYSICS

by

Christian Julienne Flacco

June 2006

Contents

List of Figures

List of Tables

Abstract

A Search for Direct *CP* Violation in Cabibbo-Suppressed Two-Body Decays of Charmed Mesons

by

Christian Julienne Flacco

Presented are the results of a search for direct *CP* violation in Cabibbo-suppressed decays of D^0 to two charged daughters. The analysis described was performed on $\sim$230 fb^{-1} of the *BABAR* data sample, recorded at the Stanford Linear Accelerator Center and using the PEP-II electron storage rings. We measure *CP* asymmetries for decay to the KK and $\pi\pi$ final states, as well as for the branching ratio, and develop a new technique for tagging-efficiency correction using the Cabibbo-favored $K\pi$ final state. We find some evidence for *CP* violation in decays to the KK final state, and results that suggest *CP* violation in the $\pi\pi$ final state as well.

To Michael, with gratitude and love

Acknowledgments

This work was supported in part by the U.S. Department of Energy under contract numbers DE-FG02-04ER41286 and DE-AC02-76SF00515.

I am grateful to the *BABAR* Collaboration for providing the scientific community in which so many graduate students learn so much.

The size of the data sample is due to the extraordinary contributions of our PEP-II colleagues in achieving excellent luminosity and machine conditions. The success of this project also relies critically on the expertise and dedication of the computing organizations that support *BABAR*.

I would like to thank my Reading Committee for reviewing my work, and particularly my advisor, Abraham Seiden, for his thoughtful approach and calm guidance.

My colleague, and now my husband, Michael Wilson has been what only such a person could be, and in all the right ways.

Finally, I am grateful to my family and friends for the many forms of support I have received over the years.

Chapter 1

Physics Motives

1.1 Introduction

1.1.1 Objective

In this work, we conduct a search for direct CP violation (a_{CP}) in Cabibbo-suppressed (CS) D^0 decays:

$$D^0 \to K^-K^+ \tag{1.1}$$

$$D^0 \to \pi^-\pi^+. \tag{1.2}$$

$$a_{CP}^{KK} = \frac{\Gamma(D^0 \to K^-K^+) - \Gamma(\bar{D}^0 \to K^-K^+)}{\Gamma(D^0 \to K^-K^+) + \Gamma(\bar{D}^0 \to K^-K^+)} \tag{1.3}$$

$$a_{CP}^{\pi\pi} = \frac{\Gamma(D^0 \to \pi^-\pi^+) - \Gamma(\bar{D}^0 \to \pi^-\pi^+)}{\Gamma(D^0 \to \pi^-\pi^+) + \Gamma(\bar{D}^0 \to \pi^-\pi^+)} \tag{1.4}$$

The ratio of these rates is also interesting, and we may also consider the asymmetry of the branching ratio of the two CS modes,

$$a_{CP}^{R} = \frac{R_{CS} - \bar{R}_{CS}}{R_{CS} + \bar{R}_{CS}}, \tag{1.5}$$

where

$$\begin{aligned} R_{CS} &= \frac{\Gamma(D^0 \to KK)}{\Gamma(D^0 \to \pi\pi)} \\ \bar{R}_{CS} &= \frac{\Gamma(\bar{D}^0 \to KK)}{\Gamma(\bar{D}^0 \to \pi\pi)}. \end{aligned} \tag{1.6}$$

We note that $a_{CP}^{R} \approx a_{CP}^{KK} - a_{CP}^{\pi\pi}$. The approximation is that terms of second order in the two CP asymmetries are negligible. This is a good approximation based on theory as well as current data. The quantity a_{CP}^{R} provides a useful consistency check due to cancellation of reconstruction efficiencies.

There are hints that we may not fully understand these decays, and this suggests that these measurements may present interesting results. The branching ratio of the two CS modes

$$\mathcal{BR}_{CS} = \frac{\Gamma(D^0 \to K^-K^+) + \Gamma(\bar{D}^0 \to K^-K^+)}{\Gamma(D^0 \to \pi^-\pi^+) + \Gamma(\bar{D}^0 \to \pi^-\pi^+)} \tag{1.7}$$

is unexpectedly high, at a measured value of 2.826±0.097 [1]. This is well above the simple estimate in the limit of flavor SU(3) symmetry, which would be unity, but also well above calculations that take flavor symmetry-breaking and phase-space considerations into account. Even with these additional considerations, this branching

ratio is not expected to exceed 1.4. Popular explanations have involved large final-state interactions, and significant penguin-level amplitude contributions. Such effects could in principle introduce CP-violating asymmetries in the rates of these decay modes.

1.1.2 The Physics of Direct CP Violation

CP non-invariance was first observed in neutral strange mesons in 1964 [2]. At that time, flavor mixing was understood to proceed among the known quarks (then two generations), and was parametrized by a single angle, θ_C. The mixing matrix was thus merely a two-dimensional real rotation matrix. With the observation of CP-symmetry breaking, a third generation of quarks was predicted, cleverly introducing an irreducible (and CP-violating) phase. This insight into generating CP violation within the known constraints of the Standard Model (SM) is known as the Kobayashi-Maskawa (KM) ansatz, and the resulting three-dimensional flavor-mixing matrix is known as the CKM matrix. This description has since been tested to the current limits of experiment, and to date remains irrefuted by the evidence.

CP-symmetry breaking is realized through interference between weak phases and thus requires that final states proceed though more than one diagram. As shown below, the presence of a strong-phase difference is also required. Specifically, we define

direct CP asymmetry thus:

$$a_{CP} \equiv \frac{|\mathcal{A}|^2 - |\bar{\mathcal{A}}|^2}{|\mathcal{A}|^2 + |\bar{\mathcal{A}}|^2}, \tag{1.8}$$

where $\mathcal{A}$ is the amplitude of a particular process, and $\bar{\mathcal{A}}$ is the amplitude of the CP-conjugate process. To shed some light on what this means for physical processes, we express the amplitudes in terms of two parts, each with a factor that changes sign under CP (such as produced by the weak phase) and a CP-invariant phase factor (such as the strong phase):

$$\begin{aligned} \mathcal{A} &= A_1 e^{i\delta_1} + A_2 e^{i\delta_2} \\ \bar{\mathcal{A}} &= A_1^* e^{i\delta_1} + A_2^* e^{i\delta_2} \end{aligned}$$

where A_i are the amplitudes of the contributing terms with the CP-invariant strong-phase factors divided out, and δ_i are the corresponding strong phases. We may now express a_{CP} in terms of these parameters.

$$a_{CP} = \frac{2\,\Im(A_1 A_2^*)\sin(\delta_2 - \delta_1)}{|A_1|^2 + |A_2|^2 + 2\,\Re(A_1 A_2^*)\cos(\delta_2 - \delta_1)}. \tag{1.9}$$

1.2 Current Theory and Predictions

CP-symmetry breaking is an intriguing subject for reasons both historical and intrinsic. Historically, what is known in the literature as the KM ansatz is an archetypal example in Particle Physics of New Physics predicted completely indirectly, from only

careful study of the behavior of known particles and keen deductive insight. Beyond this, however, CP-violation is tantalizing because it enters into the SM solely through complex phases of mass matrices, and thus is irresistibly linked with the physics of mass generation.

1.2.1 Standard Model Predictions

In principle, direct CP asymmetries are allowed for the (singly) Cabibbo-suppressed modes in the SM by the KM ansatz. This is in contrast to the Cabibbo-favored and doubly Cabibbo-suppressed cases, for which the final states are not CP eigenstates. In these non-eigenstate cases any observation of direct CP asymmetry would be a signal of New Physics.

In the case of the CS two-body modes considered here, using the KM ansatz, interference among multiple hadronization channels must be the source since the processes involve only the first two generations of quarks in the dominant quark-level diagrams. (The penguin diagram, mentioned below, is estimated on basic grounds to be a very small correction in the Standard Model.)

The general expectation from the SM is that the magnitude of the asymmetry will be $\mathcal{O}(10^{-3})$ for each mode.

There are many challenges in accurately calculating the Standard Model prediction for the quantity measured in this analysis. The charm quark mass, at the scale

Table 1.1: Phenomenological SM predictions for CP asymmetries in the CS two-body modes studied in this analysis.

$10^3 \times a_{CP}^{KK}$	$10^3 \times a_{CP}^{\pi\pi}$
0.13 ± 0.8	0.02 ± 0.01

of 1 GeV/c^2, is clearly not negligible. Yet the assumptions used in Heavy Quark Effective Theory (HQET) are also inapplicable. This is apparent in the largely different lifetimes of the charmed mesons; the charged D is more than twice as long-lived as it's neutral counterpart.

There have been some phenomenological calculations done to estimate the effects we are looking for in the Standard Model. In particular, F. Buccella and colleagues [3] have produced accurate values for the measured branching ratios of these modes, and they also provide expected values for the CP asymmetries. These are given in Table 1.1.

1.2.2 New Physics

Because the SM prediction is for so small a value, any sizable measured asymmetry would suggest New Physics. An enticement for this measurement may be found in considering the tree and penguin Feynman diagrams for the CS modes. We observe that the KK and $\pi\pi$ amplitudes have different signs in the tree level diagram (Figure 1.1). However, the main penguin contributions (Figure 1.2) to each share a

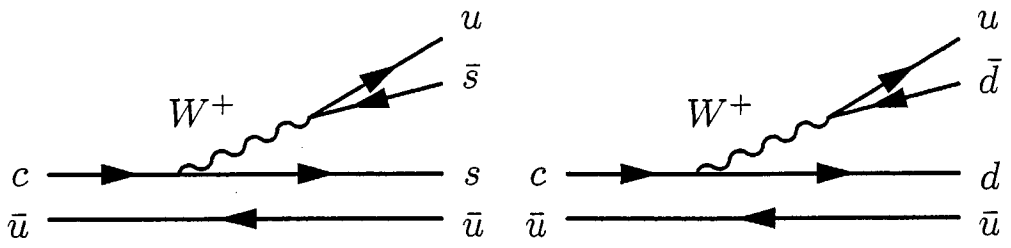

Figure 1.1: Tree-level quark diagrams contributing to the CS two-body modes, Final state KK, left; final state $\pi\pi$ right. Note that although these diagrams are topologically identical, the CS vertex is in different configurations in the two, leading to opposite overall signs for this amplitude contribution in the two modes.

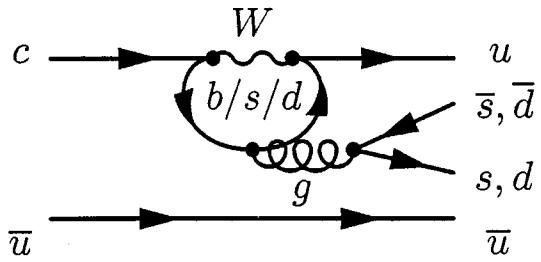

Figure 1.2: Primary penguin-level quark diagrams contributing to the CS two-body modes. Unknown contributions could enter in the loop, potentially leading to CP violation.

sign.

Thus, this contribution tends to produce divergence between the rates of the two modes. Thus, one might speculate on the possibility of New Physics contributions to the penguin terms. It is possible that unexpectedly large penguin contributions are the source of the large ratio between KK and $\pi\pi$. If this were the case, this New Physics might also produce unexpected levels of CP violation in these modes.

Table 1.2: Summary of published experimental results for CP asymmetries.

Source	a_{CP}^{KK}	$a_{CP}^{\pi\pi}$
RPP World Avg. (2004) [1]	0.005 ± 0.016	0.021 ± 0.026
CDF Collab. (2005) [4]	$0.020 \pm 0.012 \pm 0.006$	$0.010 \pm 0.013 \pm 0.006$

1.3 Summary of Published Experimental Results

The levels of CP violation in these modes are currently constrained by previous experiments to the limits given in Table 1.2. Notably, asymmetries at the level of 1% have not yet been excluded.

Chapter 2

Analysis Strategy

2.1 Overview

2.1.1 The Dataset

In this analysis we reconstruct neutral D mesons decaying to charged two-body final states in the *BABAR* detector. We use approximately $230\,\mathrm{fb}^{-1}$ of data (*BABAR* Runs 1-4, recorded circa 2000-2004) collected at and about 40 MeV below the $\Upsilon(4s)$ resonance. Although the *BABAR* experiment is designed as a B-factory, the cross section to $c\bar{c}$ coupled with the high luminosity of the PEP-II collider make this dataset extremely compelling for the study of flavor physics in the charm sector.

The sample used in this analysis has been checked for quality and consistency by the *BABAR* collaboration, of which this author is a member. Independent studies of

subsamples of the dataset have not been performed; the sample has been treated as a whole throughout all studies and analysis.

Charm events in the sample can be isolated to adequate purity by making simple cut-based selection requirements. This analysis will not make use of any sophisticated algorithms, such as Fisher discriminants or neural nets, for background suppression. This is mentioned because in measuring CP asymmetry we must be very careful not to introduce any flavor bias that we cannot correct.

2.1.2 Signal Extraction

Once we have obtained a fairly pure sample, we will fit the D^0 and $\overline{D}^0$ mass spectra in each mode of interest to extract a signal yield. We will need to ensure that this procedure does not have a flavor bias. Although we expect prominent signals in all modes, charge asymmetries in identification and misidentification rates for the various particle species prevent us from safely assuming the combinatorial backgrounds remaining in our samples will be the same for the two D^0 flavors.

Since the CS final states are identical for the D^0 and $\overline{D}^0$, there can be no asymmetry due to this reconstruction alone. Detection efficiencies for the final states particles cancel out of all the quantities we are interested in here. Another consequence of this is that the resolution of the mass spectra for CS samples is also flavor-independent (though not mode-independent). Any non-physical asymmetry caused by charge-

biased selection criteria would be introduced at the D^0 flavor-tag level. What is meant by this is described in the next section.

2.2 The Soft-Pion Flavor Tag

In reconstructing final states shared by D^0 and $\bar{D}^0$, such as the CS *CP* eigenstates to be studied here, it is necessary to use an independent means of ascertaining the flavor of the decaying neutral D-meson. That is, we need a flavor tag. Fortunately, such a tag has long been known in the charm sector. Consider the decay chain shown.

$$\begin{aligned} D^{*+} &\rightarrow \pi_s^+ \quad D^0 \\ & \qquad\quad D^0 \rightarrow K^- K^+ \end{aligned} \tag{2.1}$$

The charged-pion daughter of the D^* is noted to be *soft*, that is, from the soft (low) end of the momentum spectrum. This is because the mass difference between the D^* and D^0 mesons is rather close to the mass of a charged pion, leaving little for kinetic contributions. The importance of this will be explained shortly. The charge-conjugate chain obviously has an oppositely charged soft pion.

This particular decay chain is interesting because although the D^* itself is too short-lived to be tracked in the particle detector, it has a clear signature in the soft pion, which carries its charge. In fact, this tag is used in many analyses, even when a flavor tag is not explicitly needed, because it dramatically improves D^0-sample purity.

Having solved the problem of flavor discrimination, we turn now to the question of reconstruction efficiency. A common strategy to reduce uncertainties due to efficiency corrections is to construct ratios of quantities in which such corrections are cancelled. For example, by constructing ratios between final states that contain the same particle types, efficiency corrections due to particle identification may cancel.

In measuring a CP asymmetry, we will construct ratios with identical final-state particles. However, the flavor tags for the D^0 and $\overline{D}^0$ rely on pions of different charges. The effect we are looking for is known to be very small; thus we must pay great care to precision. Therefore, we must quantify the charge asymmetry of soft-pion detection. Because it is known to be small, we cannot rely on Monte Carlo simulation which is simply not precise to this degree.

Other experimenters (*e.g.*, the CDF Collaboration [4]) have used generic methods, which rely to a large extent on simulated data to correct for particle identification asymmetries, for calculating the charge asymmetry in their detection of pions at the low end of the momentum spectrum. They then do a systematic study of the effect of this correction by applying it to the Cabibbo-favored mode and making sure that flavor asymmetry is not artificially introduced. Of course, since the D^0 and and $\overline{D}^0$ do not have identical final states in this mode, their is an additional efficiency that must be accounted for in this method. This has been done using simulated data. It is clear that there are several sources of error in this method, and for this reason this method

has somewhat large systematic uncertainties. Since prior searches for CP violation in these modes have been severely limited by low statistics, this has not been a major concern. In our case, the statistical sensitivity of our sample requires us to develop a greater sensitivity to the asymmetry of our flavor tag.

2.3 Measuring the Soft-Pion Tagging Efficiency Precisely Using Data

To measure the relative efficiency of the flavor tags ($\epsilon_r = \epsilon^+/\epsilon^-$, where the sign is taken from the charge of the tagging π_s), we desire samples of neutral D mesons of known flavor to which we may then apply the flavor tags and study the resulting tagged sub-samples.

Such a sample is to be had in the Cabibbo-favored mode:

$$D^0 \to K^-\pi^+ \text{ (+ c.c.)} \tag{2.2}$$

In this mode the flavor information from the charmed meson is preserved in the charge of the final-state kaon. This decay channel thus provides a natural laboratory for study of the soft-pion tag. A further benefit of this channel is that it provides fairly high statistics which is important in a sample used for calculating corrections. The main challenge presented by this method is the poor purity of the sample in absence of the

flavor tag. This will be further discussed in a later chapter dedicated to the efficiency corrections.

2.4 Calculation of Results

In order to maximize the statistical power of our samples, we will apply a statistical background subtraction method [5]. Without this technique, we would have been required to perform our fits in bins of D^0 momentum, thereby reducing our sensitivity to the overall yields of the samples. This subtraction method will be described in the chapter documenting the tagging efficiency procedure, where it is first used. Once this is done, we are free to apply the efficiency correction to our CS samples. We do this in bins of tagging-π_s momentum, to account for the possibility of different spectral shapes among the different modes.

It is then trivial to calculate the observed CP asymmetry of the samples. We also calculate the CP asymmetry of the branching ratio for the KK and $\pi^+\pi^-$ final states. In this quantity, all efficiency corrections, including that for tagging, cancel to first order. We therefore calculate this ratio with and without the correction as a consistency check of our method.

Chapter 3

The *BABAR* Detector

The data used in this analysis were collected from the *BABAR* detector [6], a particle detector operating on the PEP-II asymmetric storage ring at the Stanford Linear Accelerator Center (SLAC). At this facility, an electron beam of 9.0 GeV and a positron beam of 3.1 GeV are collided. The *BABAR* detector has several component systems; those that contribute to this analysis are discussed in some detail below. For this work, there are two areas of interest: charged-track reconstruction (including at low momentum) and charged-particle identification (PID).

3.1 Track Reconstruction

Charged-track reconstruction (*i.e.* tracking) in *BABAR* proceeds through the tandem contributions of its two inner-most sub-systems: the silicon vertex tracker (SVT)

and the drift chamber (DCH). The SVT is designed to provide both vertexing capabilities and independent tracking of low-momentum charged particles. Through careful alignment and calibration, these two detectors support efficient high-precision tracking in *BABAR* over a broad momentum spectrum, detecting charged particles down to transverse momenta of $50\,\mathrm{MeV}/c$. The tracking system operates within a $1.5\,\mathrm{T}$ solenoidal magnetic field supplied by superconducting electromagnets; the steel flux return, making up the outermost layer of the *BABAR* detector, is instrumented to identify muons and detect neutral hadrons.

3.1.1 Silicon Vertex Tracker

The physics goals of *BABAR* require a single-vertex resolution of $80\,\mu\mathrm{m}$. In addition to vertex capabilities, the SVT must also provide stand-alone tracking of charged particles with low transverse momentum ($p_t < 120\,\mathrm{MeV}/c$) that will not travel far enough from the beam axis to be accurately measured in the drift chamber.

The physical constraints at the PEP-II interaction region significantly affect the design of the SVT. Permanent dipole magnets are located at a distance of $\pm 20\,\mathrm{cm}$ from the interaction point, so the SVT must be mounted on them. The magnets limit the acceptance angle of the detector to the range $17.2° < \theta < 150°$. To achieve high luminosity, bunches are spaced only $4.2\,\mathrm{ns}$ apart, meaning hit information must be buffered and the readout should be sparse. Finally, the anticipated radiation for the inner-most

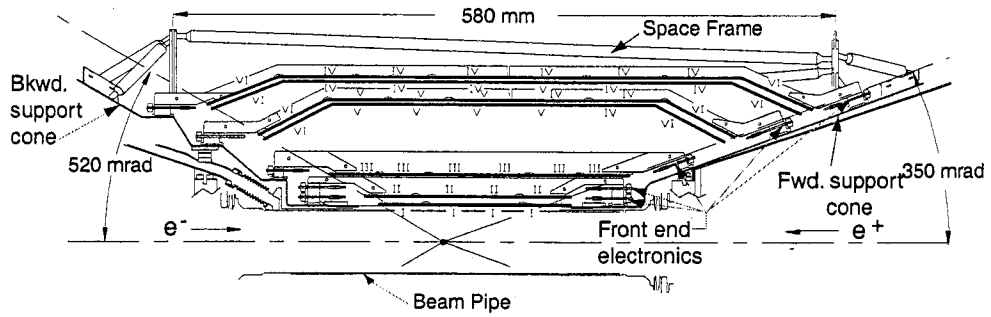

Figure 3.1: Schematic view of the SVT: longitudinal section. The roman numerals label the six different types of sensors.

layers is expected to be 250–400 kRad/yr on average and 1000–2000 kRad/yr in the horizontal bending plane of the beams (caused by the permanent dipole magnets), so the detector must be radiation hard.

The SVT consists of 5 layers of double-sided AC-coupled silicon sensors (Figure 3.1). The inner three layers are critical in providing vertex information, and we require a single-hit resolution of 10–15 μm. These sensors are arranged in a six-sided cylindrical shape. The outer two layers provide tracking information and pattern recognition that can be used with other sub-detectors or in a stand-alone manner. These outer modules are designed in an arc shape in order to minimize the amount of silicon required and to increase the crossing angle for detected particles near the edge of the acceptance region. A single-hit resolution of 30–40 μm is sufficient in these modules.

The SVT has met or exceeded all of its performance design goals. Single hit resolution for perpendicular tracks matches the design specifications: 10–15 μm for layers

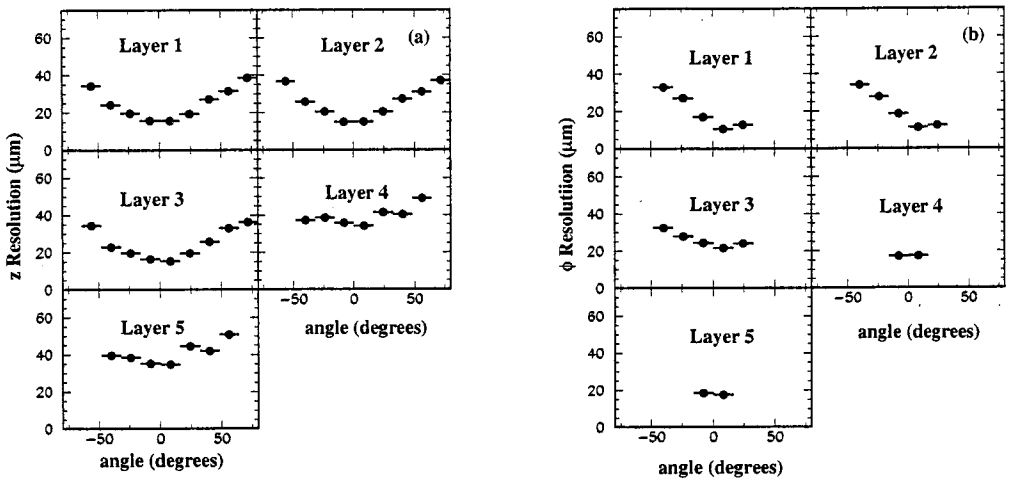

Figure 3.2: SVT hit resolutions as a function of track incidence angle: along the beam axis z (left) and perpendicular to the beam axis ϕ (right).

1–3 and 30–40 μm for layers 4–5 (Figure 3.2). Hit reconstruction is typically better than 98% for all functioning modules. Figure 3.3 (left) shows the resolution of the reconstructed track parameters d_0 and z_0, which represent the distances between the point of closest approach to the z-axis and the origin in the x-y plane and along the z-axis, respectively. Figure 3.3 (right) shows the estimated error in the measurement of the difference along the z-axis between the vertices of the two neutral B mesons, one of which is fully reconstructed. The SVT provides tracking information for particles with low transverse momentum $p_t \gtrsim 50\,\mathrm{MeV}/c$, which is important for tracking soft pions, for example from $D^{*+} \to D^0\pi^+$.

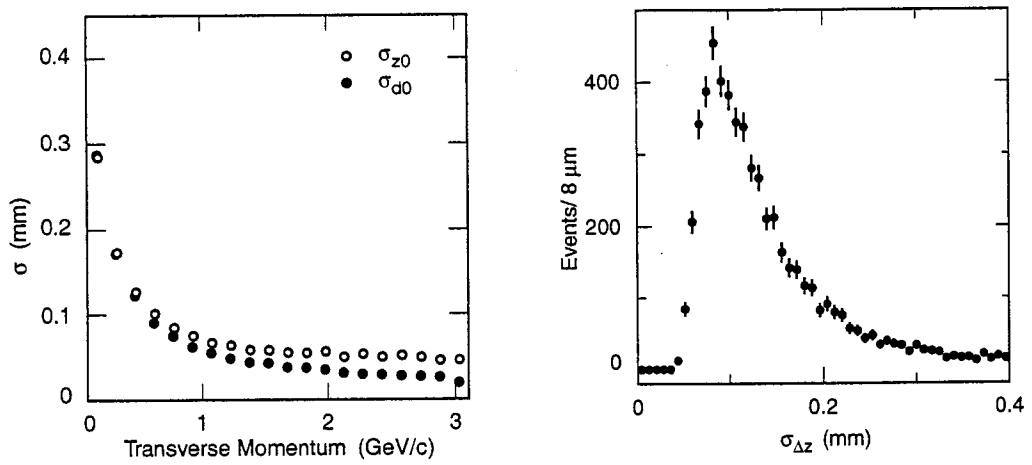

Figure 3.3: (Left) Resolution in the parameters d_0 and z_0 for tracks in multi-hadron events as a function of the transverse momentum. (Right) Distribution of the error on the difference Δz between B meson vertices, one of which is fully reconstructed.

3.1.2 Drift Chamber

The primary role of the drift chamber (DCH) is to provide high-precision momenta measurements for charged particles. This is important for low-background reconstruction of exclusive D-meson decays.

The DCH is composed of 40 layers of small hexagonal cells consisting of one sense wire surrounded by six field wires. It is relatively small in diameter, and it has a length of almost 3 m (Figure 3.4). With this geometry, charged particles with transverse momenta above 180 GeV/c may have up to 40 spatial and ionization-loss ($\mathrm{d}E/\mathrm{d}x$) measurements in this detector. The DCH also provides longitudinal spacial measurements. This capability is due to the placement of wires in 24 of the 40 layers at small angles relative to the primary axis.

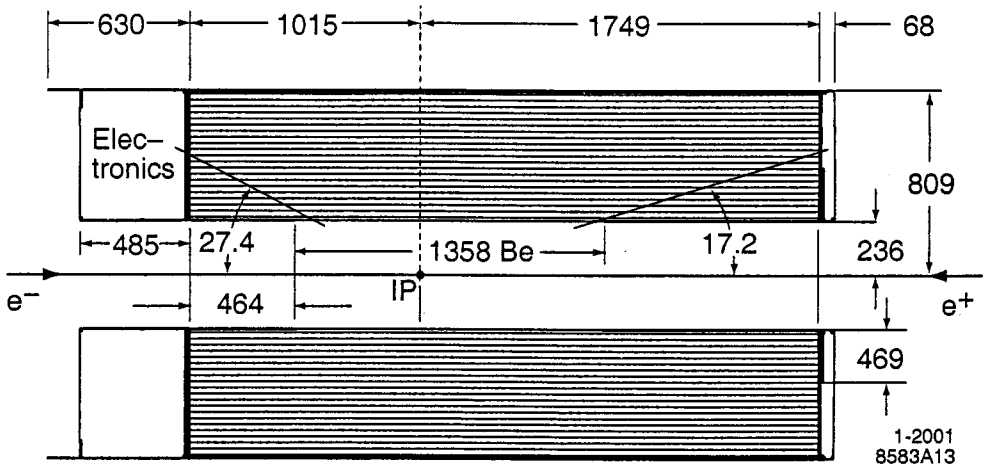

Figure 3.4: Schematic view of the DCH: longitudinal section.

To maximize the complementarity of devices, the DCH is designed with a thin inner cylindrical wall so that tracks may be matched with the SVT. This consideration applies to the outer wall as well so that performances of the outer subsystems are not compromised. The gas used in the chamber is an 80:20 mixture of helium with isobutane. This mixture yields a reduction in multiple scattering and an improvement in spatial resolution over past argon-based designs. The calibrated conversion of drift time to drift distance is determined from samples of electron and muon pairs. The effect of entrance angle has also been studied and corrected.

The DCH has performed reasonably well, and its performance is stable. In particular, it has met its design goal for intrinsic position (140 μm) and $\mathrm{d}E/\mathrm{d}x$ resolution (7%). Figure 3.5 shows $\mathrm{d}E/\mathrm{d}x$ measurements as a function of track momenta in the DCH.

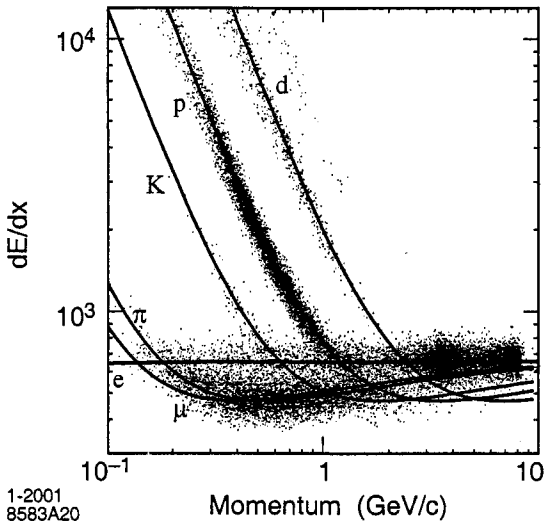

Figure 3.5: Measurement of $\mathrm{d}E/\mathrm{d}x$ in the DCH as a function of track momenta. The curves show the Bethe-Bloch predictions derived from selected control samples of particles of different masses.

3.1.3 Tracking Performance

The tracking system reconstructs charged tracks with high efficiency and sufficient resolution. The absolute DCH tracking efficiency is determined as the ratio of the number of reconstructed DCH tracks to the number of tracks detected in the SVT, with the requirement that the tracks fall within the acceptance region of the DCH. At the design voltage of 1960 V, the efficiency averages $98\%\pm1\%$ per track above 200 MeV/c and polar angle $\theta > 500$ mrad. In particular, tracking efficiency remains high for low-momentum tracks, and SVT-only tracking extends the track-finding capability down to ≈ 50 MeV/c (Figure 3.6).

Charged tracks are defined by five parameters, $(d_0, \phi_0, \omega, z_0, \tan\lambda)$, and their co-

variance matrix. The parameters (d_0, z_0) have already been defined in Section 3.1.1. The parameter ϕ_0 is the azimuthal angle of the track (defined at the point of closest approach to the origin), λ is the dip angle relative to the transverse plane, and $\omega = 1/p_t$ is the track curvature. The resolutions of these parameters can be measured using cosmic-ray tracks that pass through the detector. The cosmic-ray detector hits are fit as two separate tracks, one in each half of the detector. The differences in track parameters for the two reconstructed tracks are shown in Figure 3.7 for tracks with transverse momenta above 3 GeV/c. Based on the full width at half maximum of these distributions, the resolutions for single tracks can be parameterized as

$$\begin{aligned} \sigma_{d_0} &= 23\,\mu\mathrm{m} \\ \sigma_{z_0} &= 29\,\mu\mathrm{m} \\ \sigma_{\phi_0} &= 0.43\,\mathrm{mrad} \\ \sigma_{\tan\lambda} &= 0.53 \times 10^{-3}. \end{aligned}$$

The transverse-momentum resolution is determined to be

$$\sigma_{p_t}/p_t = (0.13 \pm 0.01)\% \cdot p_t + (0.45 \pm 0.03)\%. \tag{3.1}$$

3.2 Particle Identification

Good separation between kaons and pions is crucial for the analysis undertaken in this work. The *BABAR* detector relies on ionization-loss ($\mathrm{d}E/\mathrm{d}x$) measurements in the

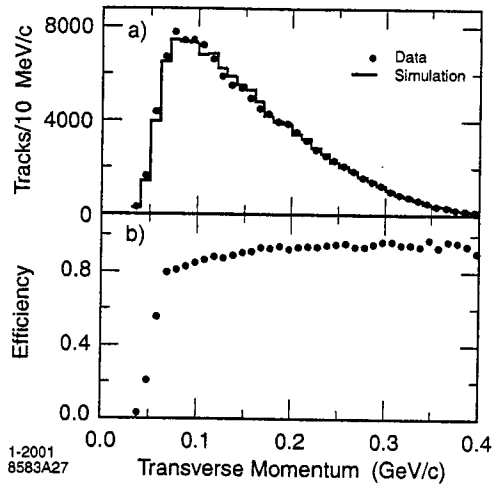

Figure 3.6: Monte Carlo studies of low momentum tracking in the SVT: a) comparison of data (contributions from combinatoric background and non-$B\overline{B}$ events have been subtracted) with simulation of the transverse momentum spectrum of pions from $D^{*+} \rightarrow D^0\pi^+$ in $B\overline{B}$ events, and b) efficiency for soft pion detection derived from simulated events.

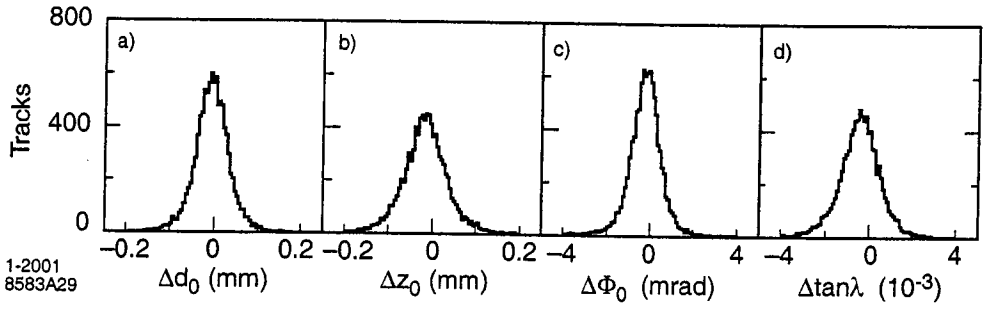

Figure 3.7: Measurements of the differences between the fitted track parameters of the two halves of cosmic ray muons, with transverse momenta above 3 GeV/c, a) Δd_0, b) Δz_0, c) $\Delta\phi_0$, and d) $\Delta \tan\lambda$.

tracking system for particle identification (PID) of low momentum tracks. For tracks with transverse momentum above 700 MeV/c, *BABAR* has a dedicated PID system, the detector of internally-reflected Cherenkov light (DIRC). The DIRC is a uniquely-designed ring-imaging Cherenkov detector, and some details are given below.

3.2.1 $\mathrm{d}E/\mathrm{d}x$ in the Tracking System

As noted above, the drift chamber can separate K from π with resolution of 7% up to 700 MeV/c (Figure 3.5). In particular, for particles traveling in the extreme backward or forward direction, this is the only discriminating information available. Measurements of $\mathrm{d}E/\mathrm{d}x$ are also available from the SVT, but in this area it plays primarily a supporting role.

3.2.2 Detector of Internally-Reflected Cherenkov Light

Above 700 MeV/c, charged particles are identified in the dedicated PID system in *BABAR*, known as the DIRC. This ring-imaging Cherenkov detector consists of 144 synthetic quartz bars oriented axially just beyond the drift chamber radially. Global design requirements mandate that the PID system must be thin and uniform to minimize resolution degradation of the calorimeter, located just outside it. Moreover, the resolution expectation of the DIRC is 4-σ separation between K and π over the range of applicable transverse momenta. Actual efficiencies and purities for particle

identification of K and π are provided in Appendix A.

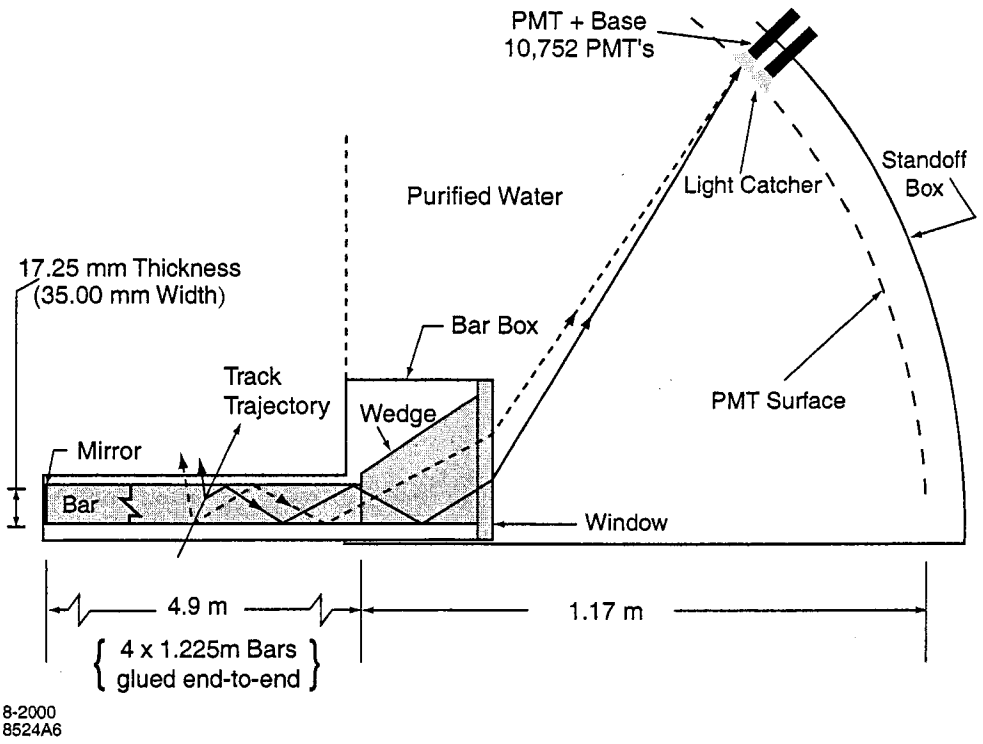

Figure 3.8: Schematic view of the DIRC fused silica radiator bar and imaging region.

A schematic of the important features of the DIRC is shown in Figure 3.8. The device is designed on the principle that reflection from a flat surface preserves angular magnitudes. The quartz bars of the DIRC serve both as radiators and as light pipes for the portion of the light trapped by total internal reflection. The material chosen for these bars has many important qualities, such as resistance to ionizing radiation, long attenuation length, large index of refraction, and an excellent optical finish on the bars themselves. These radiators are arranged in a 12-sided barrel. The asymmetry of PEP-II produces particles in a preferentially-forward direction; therefore, the DIRC

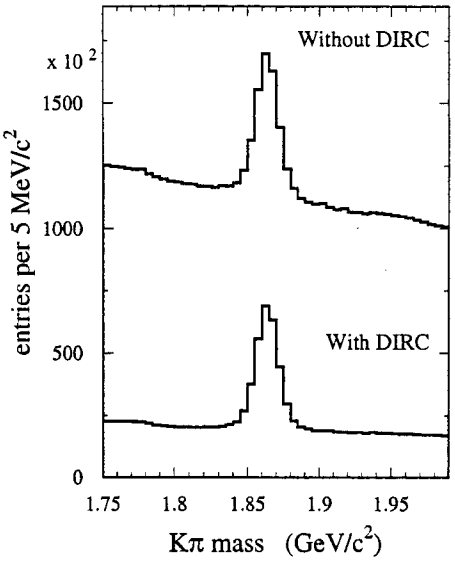

Figure 3.9: $D^0 \rightarrow K\pi$ invariant mass distribution with and without the use of the DIRC for K identification.

photon detector is placed at the backward end where it does not compete for space with front-end detecting components. Mirrors at the front end allow for this one-sided instrumentation.

The Cherenkov photons produced in the crystals are imaged by 11,000 conventional photomultiplier tubes. These are in a standoff box that contains about 6 kiloliters of purified water. Water is an inexpensive material that reasonably minimizes total internal reflection at the crystal interface. The water must be deionized and extremely pure to maintain good transparency for wavelengths down to 300 nm.

The DIRC also has a nitrogen gas system, using liquid nitrogen boil-off both to prevent condensation on the radiators and to detect water leaks.

This clever and innovative PID device has proven to be robust and stable, and it is well-matched to the hadronic-PID requirements of *BABAR*. One can appreciate the value of this system to physics analyses by considering Figure 3.9, which shows the $D^0 \rightarrow K\pi$ invariant mass distribution with and without K-identification information from the DIRC. For what concerns this analysis, the K and π misidentification rates are shown in Appendix A, Section A.2.

Chapter 4

Sample Selection

The samples used in this analysis are selected in a two-stage process. First the *BABAR* `AllEvents` data collections are filtered (known as skimming) into smaller collections meeting liberal criteria for relevance to the analysis. This is done for purely practical reasons of computing efficiency and data manageability. This smaller data set, called the `D0To2ProngDcj` skim, is then studied, refined and analyzed.

4.1 Skimming Criteria

4.1.1 D^0 Selection

The D^0 (both flavors included) candidates used in this analysis are selected with the following criteria. These criteria are fairly generic for charmed meson analyses of

BABAR data; they have been validated in previous work of the collaboration, and are well-understood and well-documented in the literature.

The basic procedure is to consider both K and π mass hypotheses for high-quality tracks recorded from the detector, and construct composite candidates from all permutations of two-track combinations. A list of resulting composite candidates is made, and includes D^0 and $\overline{D}^0$ hypotheses for the composite type. The candidates on this list are then considered against a set of criteria developed to reject known background sources and exploit basic properties of the signal source.

Selection criteria are listed:

- Refined from `SmpV0All` (a standard production list containing all permutations of two-track combinations on the `GoodTracks` production list)
- $K^{\pm}$ from `KLHTight` production list (documentation appended)
- $\pi^{\pm}$ from `piLHTight` production list (documentation appended)
- $0.005 < P(\chi^2) < 1.0$ (vertex-fit quality requirement)
- $1.7745\,\mathrm{GeV}/c^2 < m_{D^0}^{\mathrm{reco}} < 1.9545\,\mathrm{GeV}/c^2$
- $2.4\,\mathrm{GeV}/c < p_{D^0}^{\mathrm{CMS}} < 10.0\,\mathrm{GeV}/c$

4.1.2 Soft-Pion Selection

The tagging soft pion is selected primarily based on the mass of the D^* composite it produces when it is vertexed with a selected D^0. This mass is expressed in the transformed variable Δm:

$$\Delta m = m_{D^*}^{\text{reco}} - m_{D^0}^{\text{reco}}, \tag{4.1}$$

where *reco* designates that these are reconstructed candidate masses (not constrained to the mass of the assigned type). This transformation is chosen because it significantly reduces correlation with the reconstructed mass of the D^0 candidate (the correlation vanishes to first order), and it is a somewhat standard choice in this analysis sector.

Selection criteria are listed:

- π_s selected from `GoodTracksVeryLoose` production list (documentation appended)
- $0.130\,\text{GeV}/c^2 < \Delta m < 0.160\,\text{GeV}/c^2$

4.2 Post-Skim Selection

4.2.1 Additional Simple Cuts

Once the skimmed sample has been produced, we apply the following additional cuts to further reduce background. These cuts are listed, then explained below.

- Event must contain at least 4 tracks from charged particles
- $K^{\pm}$ and $\pi^{\pm}$ D^0-daughter candidate tracks must have produced at least 2 hits in each of the z and ϕ components of the SVT layers
- π_s candidate track must have produced at least 6 hits in the SVT
- $0.1434\,\mathrm{GeV}/c^2 < \Delta m < 0.1474\,\mathrm{GeV}/c^2$
- $p^{\mathrm{lab}}_{\pi_s} > 0.100\,\mathrm{GeV}/c$
- $|\cos\theta^{\mathrm{lab}}_{D^0}| < 0.8$

The event-level cut, first on the list above, is designed to eliminate combinatorial background due to $\tau^+\tau^-$ events. In practice, we find that this cut makes very little difference to the selection (affecting $\sim$0.2% of events in the presence of other cuts, with an even smaller level of asymmetry. See Figures 4.1–4.4). Since such cuts could in principle lead to uncorrected charge asymmetry, it is recommended that this cut be omitted from future analyses of this kind. The requirements for SVT hits amount to

track quality requirements. Such cuts could introduce charge-asymmetry, but these asymmetries are corrected in this analysis. Tracking asymmetries introduced at the D^0 level will cancel in ratios of identical final states. Tracking asymmetries at the D^* level are corrected by the tagging-efficiency correction procedure.

The cut on Δm is tightened significantly from that in the skim, which left large sidebands in this variable. This reduces combinatorial background significantly. The cut on π_s momentum reduces contributions from poorly reconstructed candidates. The fiducial cut on $\cos\theta_{D^0}$ is explained in Chapter 6.

4.2.2 Multiple Candidates

Once all cut-based criteria have been applied, the possibility remains of multiple candidates in an event having identical D^0 masses, but different π_s candidates. This occurrence is rare (much less than 1%). However, since we fit the D^0 mass distributions with a one-dimensional fit, we would prefer not to have multiples of this kind in the spectrum. When we find multiple D^* candidates *of the same charge*, we select the one with the value of Δm closest to the accepted value. This leaves at most one candidate of each flavor per event, without the potential introduction of a significant charge bias.

4.3 Comments on the Selection and Samples

The set of selection criteria used in this analysis are documented in Figures 4.1–4.24. In these figures, data are shown alongside simulated (Monte Carlo) events scaled to the equivalent luminosity. Monte Carlo events have been classified according to categories in which they were known to be generated (*i.e.*, events have been truth matched). All selection criteria were identically applied to both CS modes and the CF mode (with no regard to flavor). In addition, all criteria not explicitly requiring a π_s candidate were also applied to the CF control sample. Thus, the spectral characteristics of the D^0 sample is preserved as much as possible, maximizing sensitivity to the effects of the flavor tag. Cuts not applied to this last sample are considered to comprise the soft-pion tag.

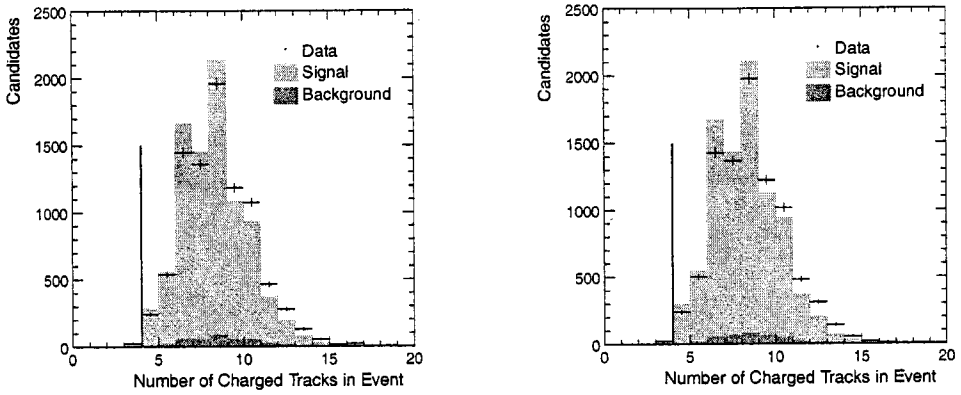

Figure 4.1: The number of tracks in the event (*i.e.*, candidates in the `GoodTracksVeryLoose` list) for the $D^0 \to K^-\pi^+$ (tagged) sample shown separately for D^0 candidates (left) and $\overline{D}^0$ candidates (right), using approximately 5 fb^{-1} of data and an equivalent number of weighted Monte Carlo events. The vertical line in each plot shows the selection cut made on that distribution. All other selection cuts except those on the distributions shown have been applied. Monte Carlo events have been truth matched.

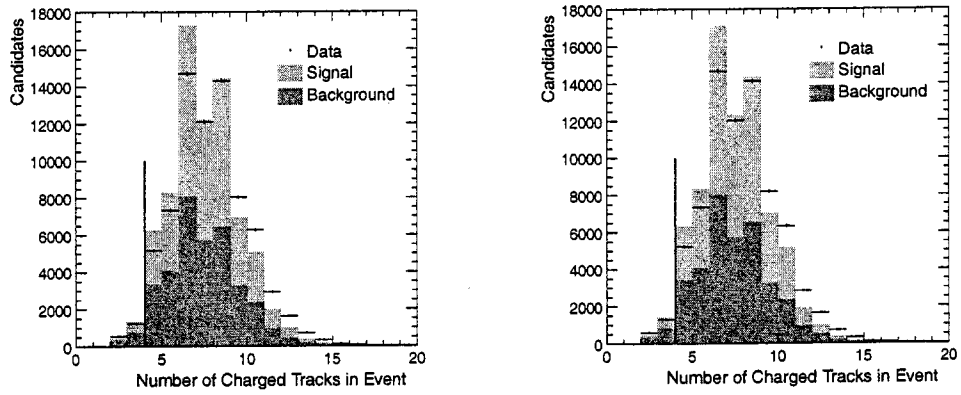

Figure 4.2: The number of tracks in the event (*i.e.*, candidates in the `GoodTracksVeryLoose` list) for the $D^0 \to K^-\pi^+$ (untagged) sample shown separately for D^0 candidates (left) and $\overline{D}^0$ candidates (right), using approximately 5 fb^{-1} of data and an equivalent number of weighted Monte Carlo events. The vertical line in each plot shows the selection cut made on that distribution. All other selection cuts except those on the distributions shown have been applied. Monte Carlo events have been truth matched.

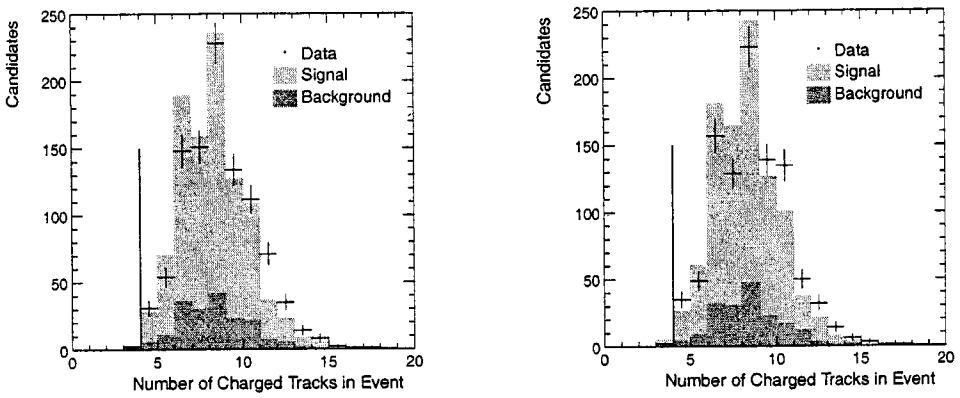

Figure 4.3: The number of tracks in the event (*i.e.*, candidates in the `GoodTracksVeryLoose` list) for the $D^0 \to K^-K^+$ sample shown separately for D^0 candidates (left) and $\overline{D}^0$ candidates (right), using approximately $5\,\text{fb}^{-1}$ of data and an equivalent number of weighted Monte Carlo events. The vertical line in each plot shows the selection cut made on that distribution. All other selection cuts except those on the distributions shown have been applied. Monte Carlo events have been truth matched.

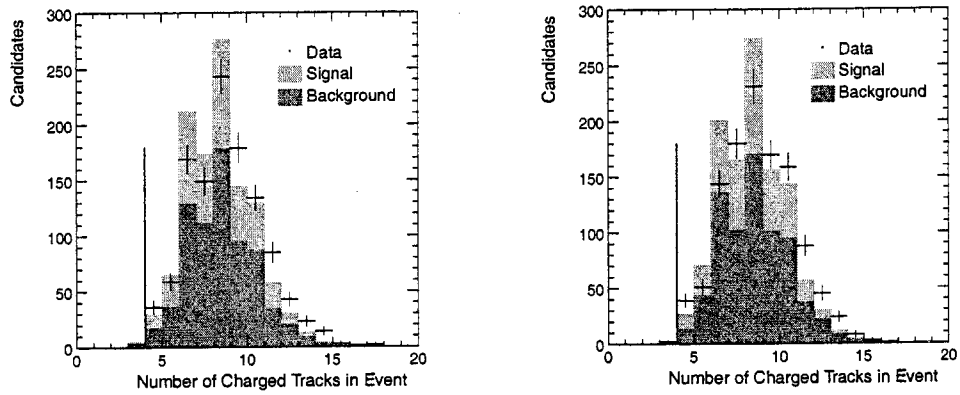

Figure 4.4: The number of tracks in the event (*i.e.*, candidates in the `GoodTracksVeryLoose` list) for the $D^0 \to \pi^-\pi^+$ sample shown separately for D^0 candidates (left) and $\overline{D}^0$ candidates (right), using approximately $5\,\text{fb}^{-1}$ of data and an equivalent number of weighted Monte Carlo events. The vertical line in each plot shows the selection cut made on that distribution. All other selection cuts except those on the distributions shown have been applied. Monte Carlo events have been truth matched.

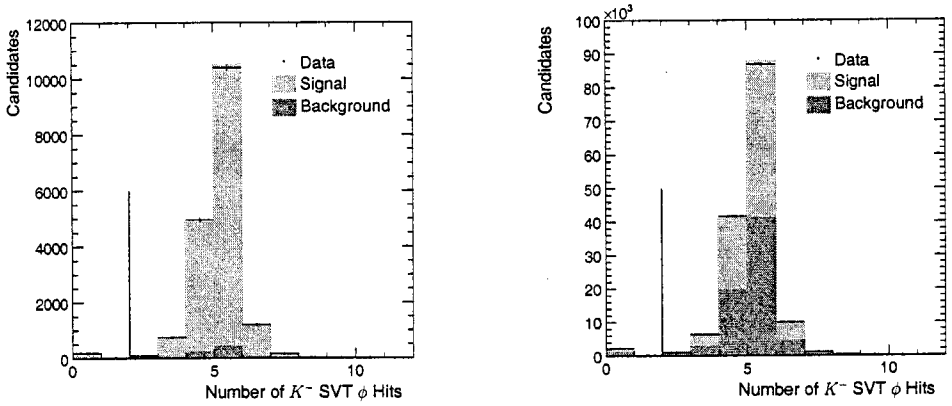

Figure 4.5: The number of azimuthal (ϕ) hits in the SVT for K candidates in the tagged (left) and untagged (right) decay $D^0 \to K^-\pi^+$ samples, using approximately 5 fb^{-1} of data and an equivalent number of weighted Monte Carlo events. The vertical line in each plot shows the selection cut made on that distribution. All other selection cuts except those on the distributions shown have been applied. Monte Carlo events have been truth matched.

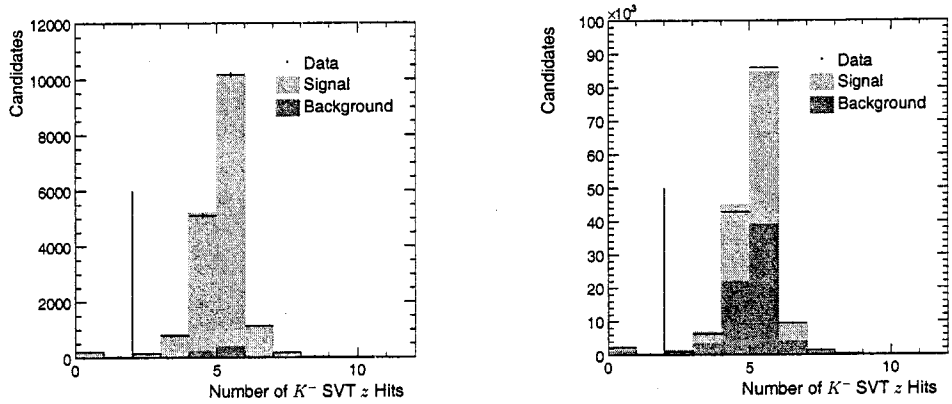

Figure 4.6: The number of axial (z) hits in the SVT for K candidates in the tagged (left) and untagged (right) decay $D^0 \to K^-\pi^+$ samples, using approximately 5 fb^{-1} of data and an equivalent number of weighted Monte Carlo events. The vertical line in each plot shows the selection cut made on that distribution. All other selection cuts except those on the distributions shown have been applied. Monte Carlo events have been truth matched.

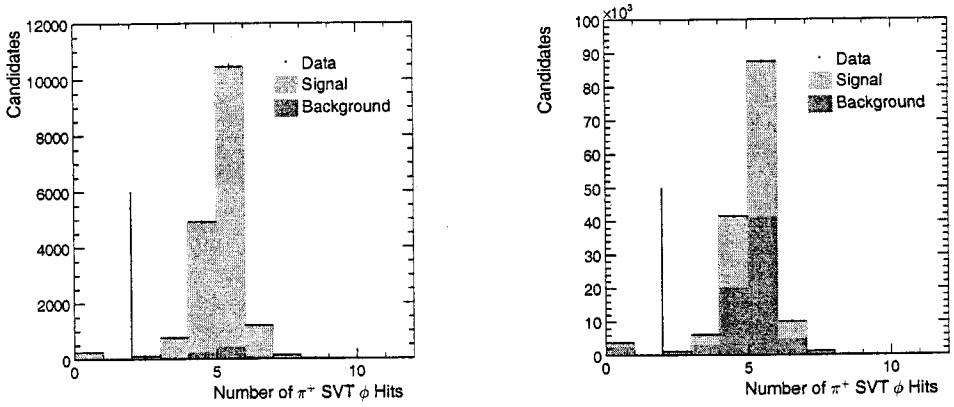

Figure 4.7: The number of azimuthal (ϕ) hits in the SVT for π candidates in the tagged (left) and untagged (right) decay $D^0 \rightarrow K^-\pi^+$ samples, using approximately 5 fb^{-1} of data and an equivalent number of weighted Monte Carlo events. The vertical line in each plot shows the selection cut made on that distribution. All other selection cuts except those on the distributions shown have been applied. Monte Carlo events have been truth matched.

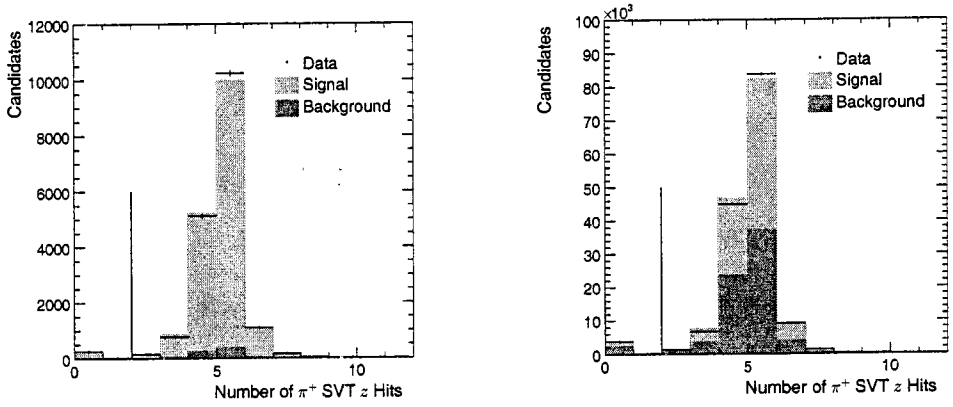

Figure 4.8: The number of axial (z) hits in the SVT for π candidates in the tagged (left) and untagged (right) decay $D^0 \rightarrow K^-\pi^+$ samples, using approximately 5 fb^{-1} of data and an equivalent number of weighted Monte Carlo events. The vertical line in each plot shows the selection cut made on that distribution. All other selection cuts except those on the distributions shown have been applied. Monte Carlo events have been truth matched.

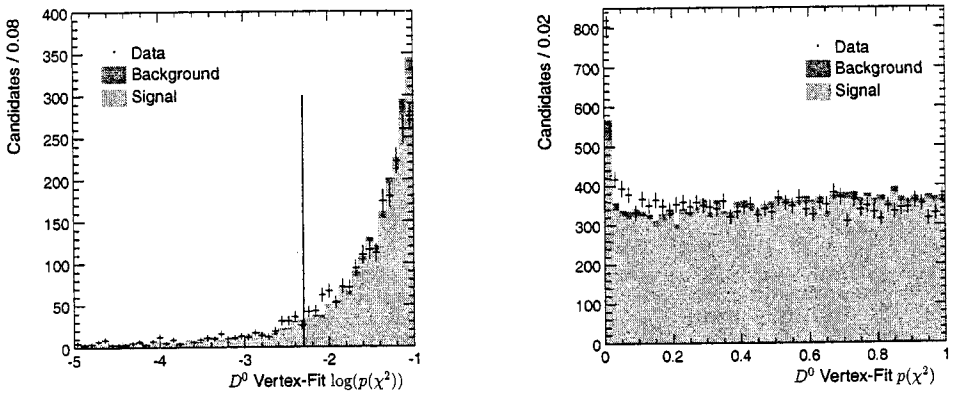

Figure 4.9: The $D^0 \to K^-\pi^+$ (tagged) vertex-fit χ^2 probability shown on a log scale (left) and a linear scale (right), using approximately 5 fb^{-1} of data and an equivalent number of weighted Monte Carlo events. The vertical line in the left plot shows the selection cut made on that distribution. All other selection cuts except that on this distribution have been applied. Monte Carlo events have been truth matched.

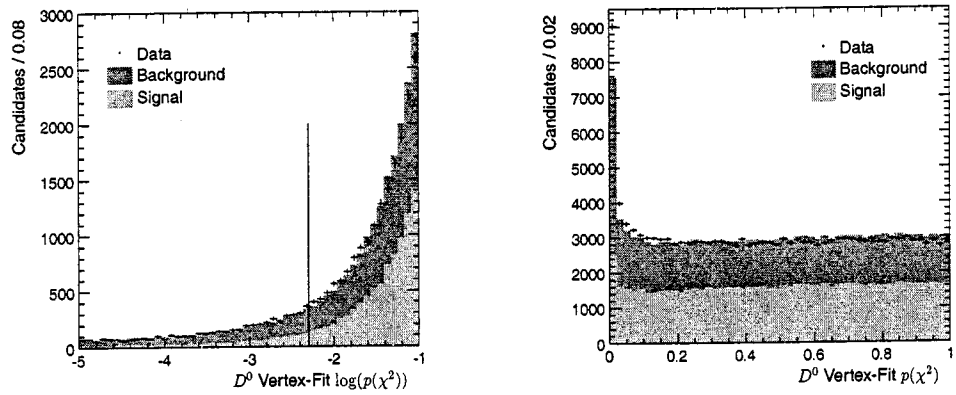

Figure 4.10: The $D^0 \to K^-\pi^+$ (untagged) vertex-fit χ^2 probability shown on a log scale (left) and a linear scale (right), using approximately 5 fb^{-1} of data and an equivalent number of weighted Monte Carlo events. The vertical line in the left plot shows the selection cut made on that distribution. All other selection cuts except that on this distribution have been applied. Monte Carlo events have been truth matched.

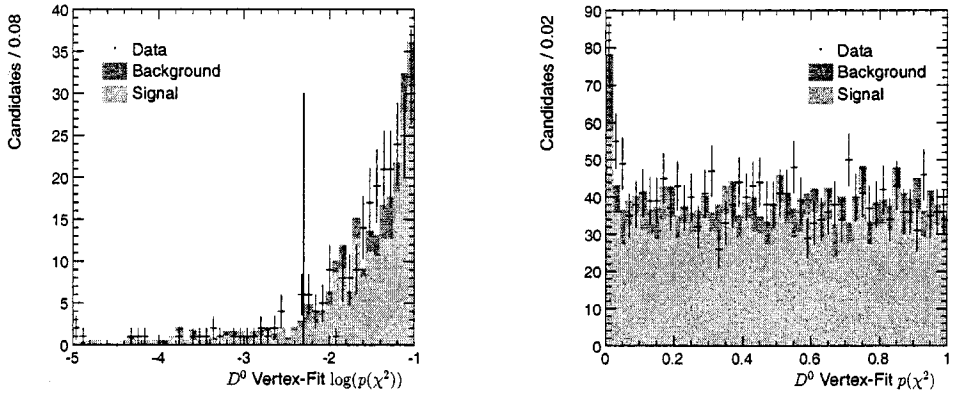

Figure 4.11: The $D^0 \to K^-K^+$ vertex-fit χ^2 probability shown on a log scale (left) and a linear scale (right), using approximately 5 fb^{-1} of data and an equivalent number of weighted Monte Carlo events. The vertical line in the left plot shows the selection cut made on that distribution. All other selection cuts except that on this distribution have been applied. Monte Carlo events have been truth matched.

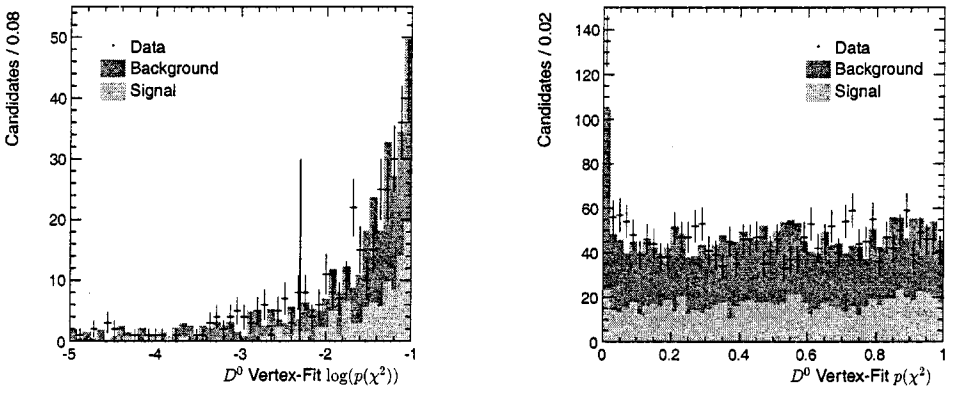

Figure 4.12: The $D^0 \to \pi^-\pi^+$ vertex-fit χ^2 probability shown on a log scale (left) and a linear scale (right), using approximately 5 fb^{-1} of data and an equivalent number of weighted Monte Carlo events. The vertical line in the left plot shows the selection cut made on that distribution. All other selection cuts except that on this distribution have been applied. Monte Carlo events have been truth matched.

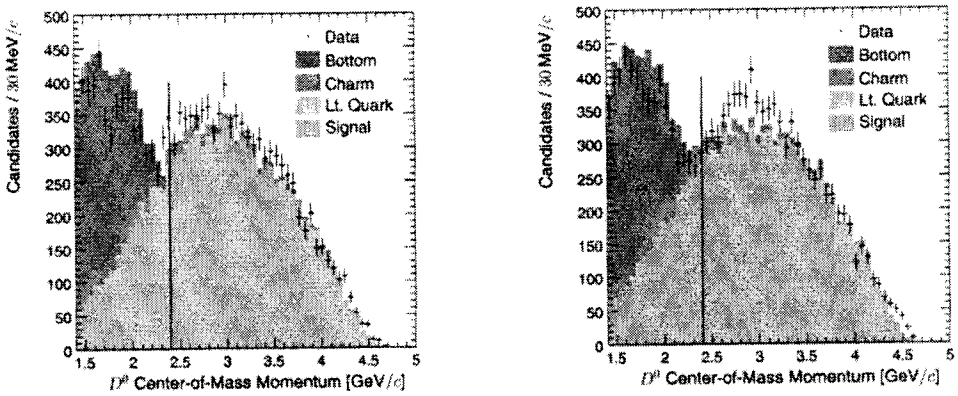

Figure 4.13: The D^0 center-of-mass momentum for the $D^0 \to K^-\pi^+$ (tagged) sample shown separately for D^0 candidates (left) and $\overline{D}^0$ candidates (right), using approximately 5 fb^{-1} of data and an equivalent number of weighted Monte Carlo events. The vertical lines in the these plots show the selection cuts made on these distributions. All other selection cuts except those on these distributions have been applied. Monte Carlo events have been truth matched.

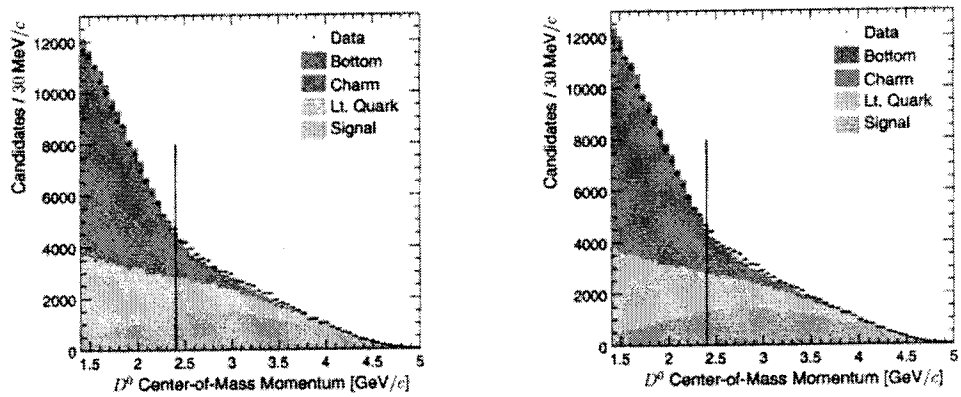

Figure 4.14: The D^0 center-of-mass momentum for the $D^0 \to K^-\pi^+$ (untagged) sample shown separately for D^0 candidates (left) and $\overline{D}^0$ candidates (right), using approximately 5 fb^{-1} of data and an equivalent number of weighted Monte Carlo events. The vertical lines in the these plots show the selection cuts made on these distributions. All other selection cuts except those on these distributions have been applied. Monte Carlo events have been truth matched.

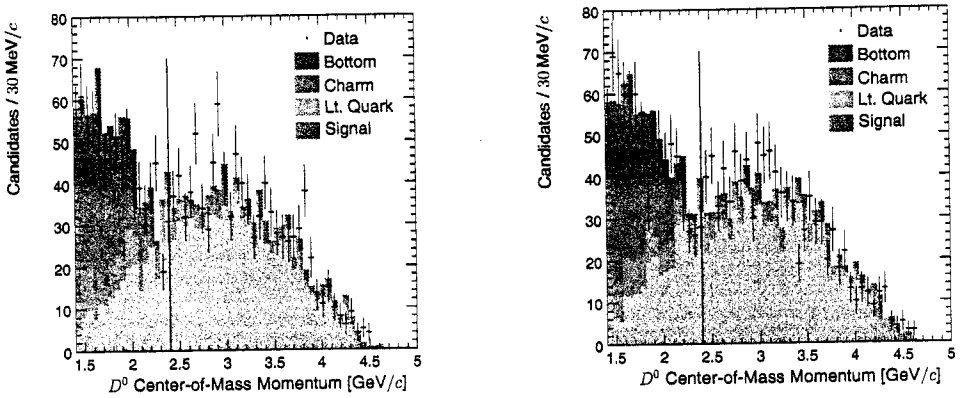

Figure 4.15: The D^0 center-of-mass momentum for the $D^0 \to K^-K^+$ sample shown separately for D^0 candidates (left) and $\overline{D}^0$ candidates (right), using approximately 5 fb^{-1} of data and an equivalent number of weighted Monte Carlo events. The vertical lines in the these plots show the selection cuts made on these distributions. All other selection cuts except those on these distributions have been applied. Monte Carlo events have been truth matched.

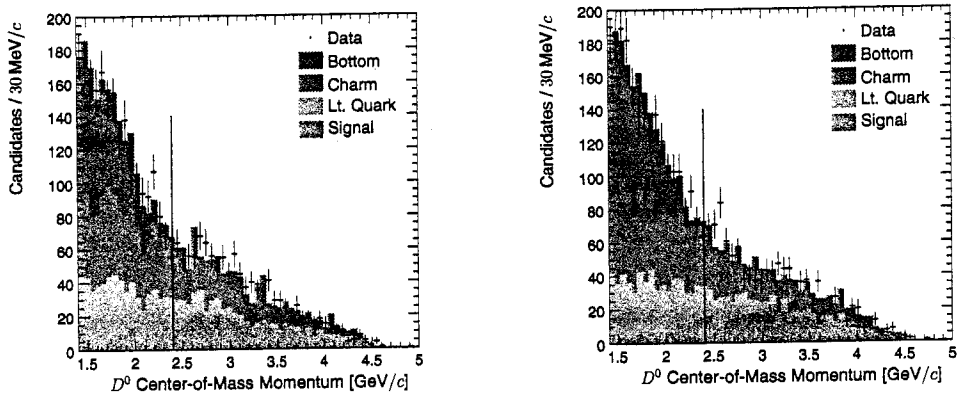

Figure 4.16: The D^0 center-of-mass momentum for the $D^0 \to \pi^-\pi^+$ sample shown separately for D^0 candidates (left) and $\overline{D}^0$ candidates (right), using approximately 5 fb^{-1} of data and an equivalent number of weighted Monte Carlo events. The vertical lines in the these plots show the selection cuts made on these distributions. All other selection cuts except those on these distributions have been applied. Monte Carlo events have been truth matched.

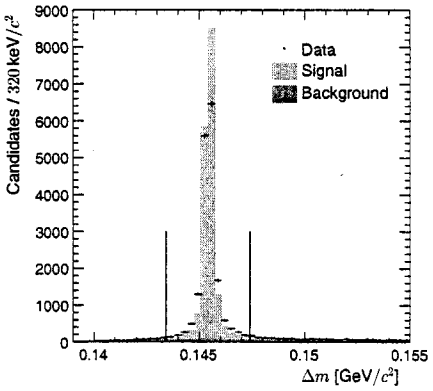

Figure 4.17: The Δm distribution for the $D^0 \to K^-\pi^+$ sample, using approximately $5\,\text{fb}^{-1}$ of data and an equivalent number of weighted Monte Carlo events. The vertical lines in the these plots show the selection cuts made on these distributions. All other selection cuts except those on these distributions have been applied. Monte Carlo events have been truth matched.

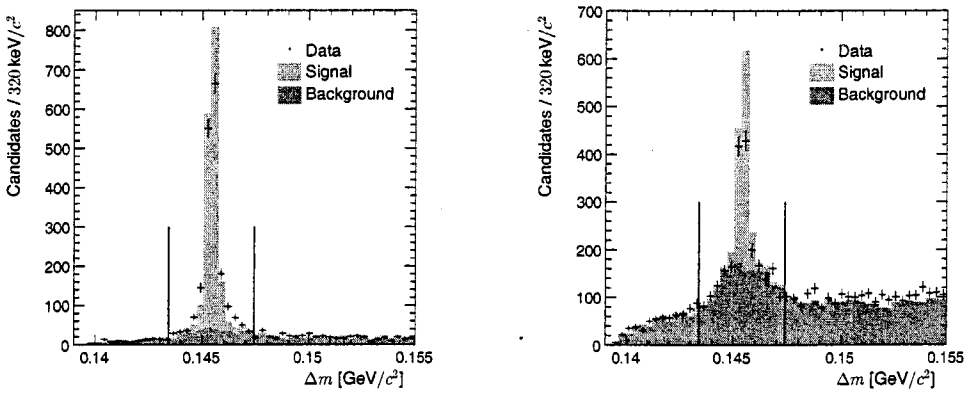

Figure 4.18: The Δm distribution for the $D^0 \to K^-K^+$ sample (left) and the $D^0 \to \pi^-\pi^+$ sample (right), using approximately $5\,\text{fb}^{-1}$ of data and an equivalent number of weighted Monte Carlo events. The vertical lines in the these plots show the selection cuts made on these distributions. All other selection cuts except those on these distributions have been applied. Monte Carlo events have been truth matched.

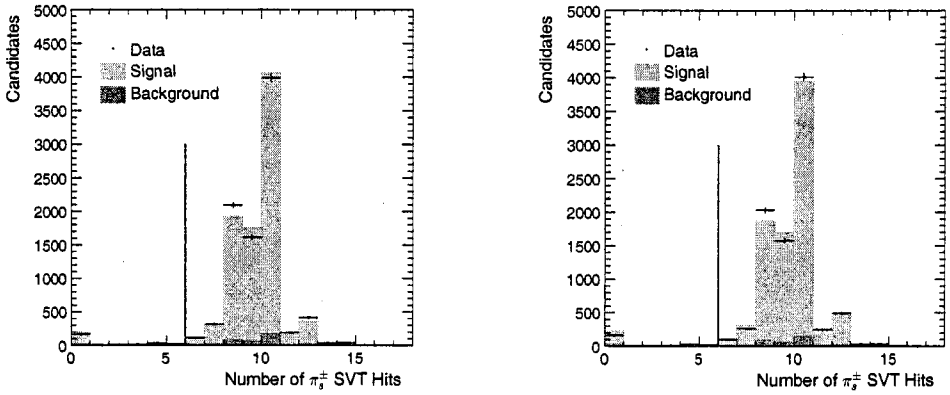

Figure 4.19: The number of hits in the SVT for $\pi_s^\pm$ candidates in the $D^0 \to K^-\pi^+$ sample shown separately for D^0 candidates (left) and $\overline{D}^0$ candidates (right), using approximately 5 fb^{-1} of data and an equivalent number of weighted Monte Carlo events. The vertical line in each plot shows the selection cut made on that distribution. All other selection cuts except those on the distributions shown have been applied. Monte Carlo events have been truth matched.

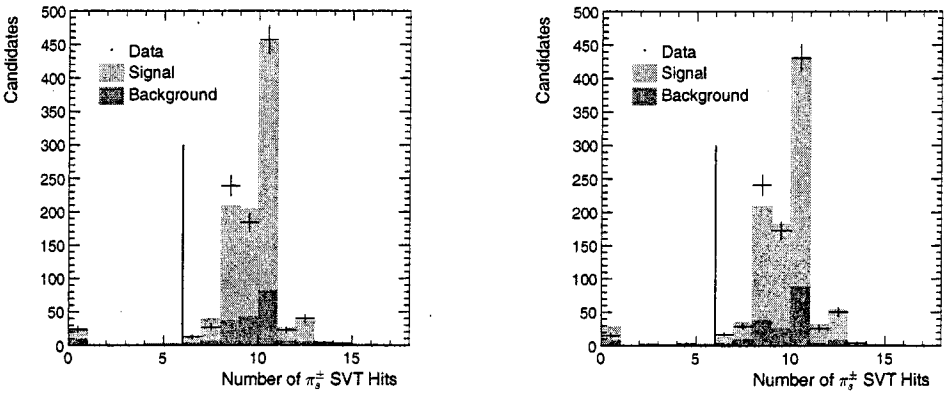

Figure 4.20: The number of hits in the SVT for $\pi_s^\pm$ candidates in the $D^0 \to K^-K^+$ sample shown separately for D^0 candidates (left) and $\overline{D}^0$ candidates (right), using approximately 5 fb^{-1} of data and an equivalent number of weighted Monte Carlo events. The vertical line in each plot shows the selection cut made on that distribution. All other selection cuts except those on the distributions shown have been applied. Monte Carlo events have been truth matched.

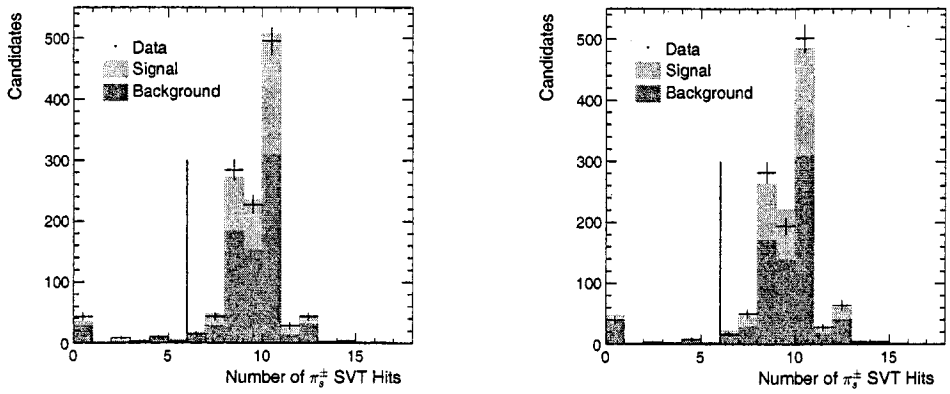

Figure 4.21: The number of hits in the SVT for $\pi_s^\pm$ candidates in the $D^0 \to \pi^-\pi^+$ sample shown separately for D^0 candidates (left) and $\overline{D}^0$ candidates (right), using approximately 5 fb^{-1} of data and an equivalent number of weighted Monte Carlo events. The vertical line in each plot shows the selection cut made on that distribution. All other selection cuts except those on the distributions shown have been applied. Monte Carlo events have been truth matched.

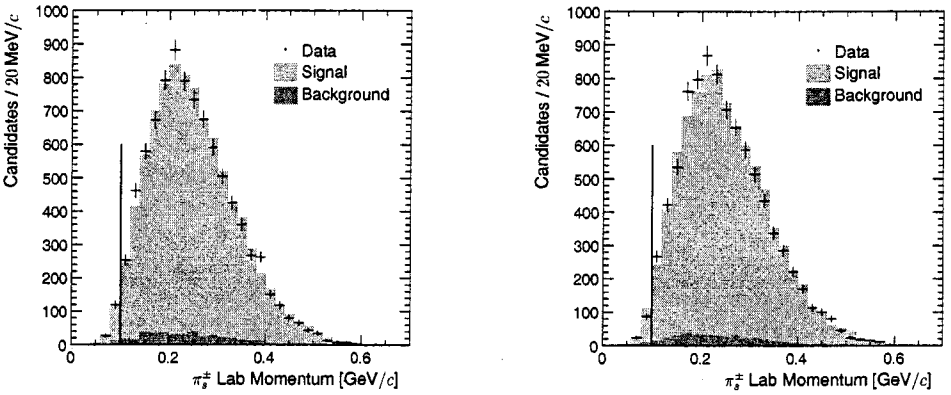

Figure 4.22: The $\pi_s^\pm$ lab momentum for the $D^0 \to K^-\pi^+$ sample shown separately for D^0 candidates (left) and $\overline{D}^0$ candidates (right), using approximately 5 fb^{-1} of data and an equivalent number of weighted Monte Carlo events. The vertical lines in the these plots show the selection cuts made on these distributions. All other selection cuts except those on these distributions have been applied. Monte Carlo events have been truth matched.

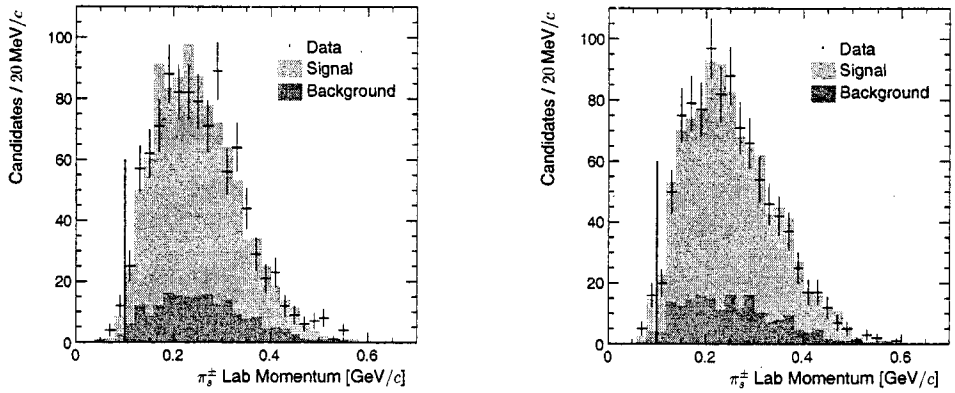

Figure 4.23: The $\pi_s^\pm$ lab momentum for the $D^0 \to K^-K^+$ sample shown separately for D^0 candidates (left) and $\overline{D}^0$ candidates (right), using approximately 5 fb^{-1} of data and an equivalent number of weighted Monte Carlo events. The vertical lines in the these plots show the selection cuts made on these distributions. All other selection cuts except those on these distributions have been applied. Monte Carlo events have been truth matched.

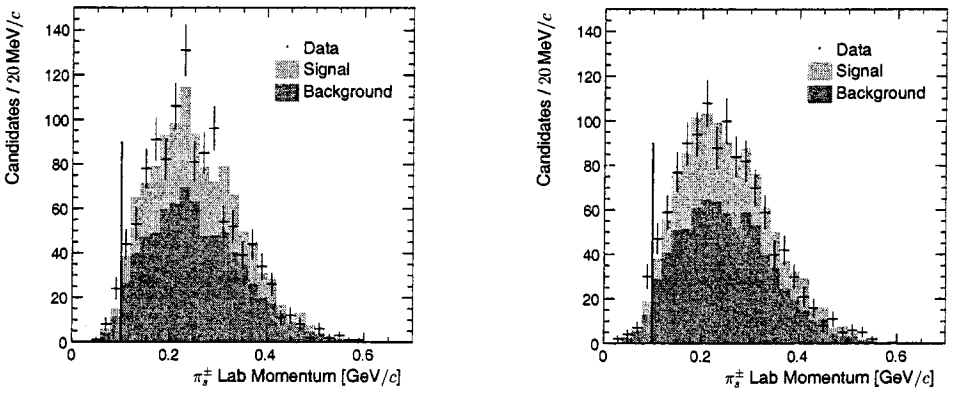

Figure 4.24: The $\pi_s^\pm$ lab momentum for the $D^0 \to \pi^-\pi^+$ sample shown separately for D^0 candidates (left) and $\overline{D}^0$ candidates (right), using approximately 5 fb^{-1} of data and an equivalent number of weighted Monte Carlo events. The vertical lines in the these plots show the selection cuts made on these distributions. All other selection cuts except those on these distributions have been applied. Monte Carlo events have been truth matched.

Chapter 5

The D^0-Mass Fit

5.1 The Maximum Likelihood Technique

The technique known as Maximum Likelihood (ML) fitting is based on the fairly simple idea that if a sample of data is composed of a finite number of exclusive categories, and these categories have distinguishable properties, then it is possible to use statistical techniques to determine the relative contributions of each category to the total sample.

Ours is a fairly simple case. We have only two categories: signal and combinatorial background. The distinguishing properties are the dissimilar statistical distributions of candidate D^0 mass that these two different categories produce. We know that the signal distribution will be clearly peaked in the region of the physical D^0 mass.

The physical width of the distribution is small compared to the detector resolution because this is a sufficiently long-lived particle ($\tau_{D^0} = 0.4$ ps). Our task is thus to select a peaking shape that accurately describes the *BABAR* reconstruction resolution for this species. By contrast, the combinatorial background category does not preferentially populate the D^0 mass region, and thus is sufficiently orthogonal to the signal category to be distinguished.

The situation would be somewhat subtler in the presence of a background source that peaked in the D^0 mass region. Such a source would be due to a physical process which tended to produce reconstructed candidates near the mass of the D^0. There are two main causes of this: mistaken identification of daughters from a physical process that mimics a reconstructed D^0 in the sample, and a decay of a heavier particle mimicking a D^0 when one of its daughters is undetected (commonly a neutral pion, for example). Peaks caused in these ways are known as reflections, and they can cause distortions to the signal, or in the worst cases simply contribute directly to the signal, and require more sophisticated category characterization (perhaps by introduction of additional variables). Fortunately, the mass spectra in this analysis have been well-studied for some time, and are known not to exhibit such artifacts from other processes in the region of the D^0 mass, although the CS modes do have reflections from the CF mode in their sidebands. This will be discussed further.

The formalism used in ML fits is the following. A function, representing the

statistical likelihood of the data sample, is constructed from probability density functions designed to characterize the categories present in the sample. The structure of the function accounts for the Poissonian statistics of counting measurements. The likelihood function for our situation, as described above is expressed in the form

$$\mathcal{L}\left(\{m_i^{\rm reco}\}, \vec{a}, n_{\rm sig}, n_{\rm bkg}\right) = \frac{\exp\{-(n_{\rm sig}+n_{\rm bkg})\}}{N!}\prod_{i=1}^{N}\{n_{\rm sig}\mathcal{P}_{\rm sig}(m_i^{\rm reco},\vec{a}) + n_{\rm bkg}\mathcal{P}_{\rm bkg}(m_i^{\rm reco},\vec{a})\}, \quad (5.1)$$

where $m_i^{\rm reco}$ is the reconstructed mass of the $i^{\rm th}$ neutral D candidate, $\{m_i^{\rm reco}\}$ is the set of all such reconstructed masses in the sample, $\vec{a}$ is the vector of parameters describing the PDF, $n_{\rm cat}$ is the hypothetical numbers of candidates in the designated category, N is the total number of events in the sample, and $\mathcal{P}_{\rm cat}$ is the normalized probability density describing the distribution of the designated category.

The values of the parameters $\vec{a}$ and the $n_{\rm cat}$ for which the function $\mathcal{L}$ is maximized represent the best statistical match of the PDF shapes to the data.

5.2 The Probability Density Functions Used

5.2.1 Signal and Background Shapes

As mentioned above, the signal shape we observe is due not to the physical D^0 lineshape, but rather to the detector resolution of *BABAR*. The overall resolution has

many contributing factors, and is not well-understood from the perspective of theoretical modelling. Thus, we turn instead to empirical models, and test our results against established standards for goodness of fit. Such a procedure is quite adequate for analyses that do not set about to measure masses or widths, but are concerned only with counting events of one kind or another.

The criteria for goodness of fit are based on the quality measures known as pull distributions. Pull distributions compare the deviation of the fit from the data sample, in units of the uncertainty on the measurements. The two features of interest are the degree of deviation, and the structure of deviations. A good fit will not have departures beyond a few standard deviations, and will exhibit no structure, that is, departures will fluctuate randomly about zero.

To perfectly model the resolution of the detector, we would like to fit for contributions from a series of Gaussian distributions. Absent any other information at all, this would be an infinite series with every imaginable combination of widths and means. (Indeed, the different resolution components need not have the same mean mass, and in fact they do not.) Fortunately, we have some knowledge of the range of contributions in our actual detector; however, even knowing this, we are faced with too many parameters for reliable fit convergence. To facilitate convergence, we select a functional form that is itself composed of many variously wide Gaussians. By judicious choice of width contributions, we may approximate the physical spectrum of

widths, while significantly reducing the number of parameters needed. Once such a form is established, a sum of such functions can accommodate the asymmetry caused by varying offsets.

In the following description of functional forms, the shapes will be expressed with arbitrary normalization for simplicity. In constructing the actual PDF terms, $\mathcal{P}_{\text{cat}}$, the functional shape f is weighted by a normalization factor appropriate to the fit range for which it is used.

Consider a function composed of many Gaussian distributions of varying widths:

$$f(x;\overline{x},\sigma_a,\sigma_b) = \int_{\sigma_a}^{\sigma_b} d\sigma \rho(\sigma) e^{\frac{-(x-\overline{x})^2}{2\sigma^2}}.$$

The limits of integration above represent the physical range of resolution contributions in the detector. We now need a width distribution, $\rho(\sigma)$. This need not be exact, since we may sum over more than one of these shapes to model the observed asymmetry due to varying offsets mentioned before.

A mathematically convenient choice for $\rho(\sigma)$ will yield an analytic integral and a functional form that tends to produce convergent fits. We have made the following choice:

$$f_1(x;\overline{x},\sigma_a,\sigma_b) = \int_{\sigma_a}^{\sigma_b} \frac{d\sigma}{\sigma^3} e^{\frac{-(x-\overline{x})^2}{2\sigma^2}}.$$

This choice is indeed analytically integrable, and physically it represents our expectation for the general trend of the resolution contributions, which we expect to have

a skew away from zero (*i.e.*, the distribution is nonnegative with a tail toward large values, and the peak value is less than the mean).

With a variable transformation, we will have the functional form used to describe the signal category in the fit. We define

$$\sigma^2 = \sigma_a \sigma_b, \quad r = \frac{\sigma_a}{\sigma_b}.$$

This transformation is made to facilitate convergence of the ML fit by changing the correlation of the parameters. After simplifying, we are left with the following functional form:

$$\mathcal{G}(x; \overline{x}, \sigma, r) = \frac{1}{(x-\overline{x})^2} \left\{ \exp\left[-\frac{1}{2} \frac{(x-\overline{x})^2}{r\sigma^2} \right] - \exp\left[-\frac{1}{2} \frac{(x-\overline{x})^2 r}{\sigma^2} \right] \right\}. \quad (5.2)$$

For the signal category of our samples we have chosen a two-term linear combination of these shapes, for the overall functional form

$$f_{\text{sig}} = c_1 \, \mathcal{G}(x; \overline{x}_1, \sigma_1, r_1) + c_2 \, \mathcal{G}(x; \overline{x}_2, \sigma_2, r_2), \quad (5.3)$$

where c_i represent the proportion of each term to the overall signal shape. All of the parameters above will be allowed to vary in the fitting procedure, subject to normalization constraints.

The background category presents much less of a challenge. We model it with a first-order polynomial (a line). This is adequate over the width of the intervals we are interested in; it has been used successfully in previous analysis of these modes performed by the *BABAR* Collaboration [7].

5.2.2 Simultaneous Fits

Although the resolution for reconstructing different final states is expected to vary somewhat, for a particular mode, we expect the signal shape for D^0 and $\overline{D}^0$ to be the same. Certainly this must true of the CS modes since the final states are shared by D^0 and $\overline{D}^0$ and this mass resolution is not correlated with the soft pion charge. In the CF case, the resolution of the D mass could be flavor-dependent to the extent that the K and π charges affect the D mass resolution. This effect is expected to be negligibly small, and cross checks of this effect are reported in a later chapter. Thus, to make the most of our sample sizes, we perform simultaneous fits of the two flavor samples to determine the signal shape parameters, allowing the yields in the two samples to differ, as well as the background shape parameters (since the two flavor samples may have different sources contributing to their combinatorial spectra).

Thus a total of four ML fits are performed on the eight samples. In each of these four fits, there are 13 parameters, all of which are allowed to vary during the minimization process: 7 signal-shape parameters, representing two means, two widths, two width ratios, and one relative fraction; two background-shape parameters, representing the linear slopes for the D^0 and $\overline{D}^0$ backgrounds; and four category yields, representing the number of signal and background events in the D^0 and $\overline{D}^0$ samples. The results of these fits are presented at the end of this chapter.

5.3 Selection of Fit Ranges

For each sample, a fit range was chosen with the following considerations. For the CS modes, ratios are to be taken between flavor samples; thus a range was chosen for each mode and used on both flavors of D^0. In these modes, the primary concern is the presence of the reflections from the CF mode. Our strategy is to choose mass ranges for the fits that effectively exclude these reflections. In the KK-mass spectra, this reflection appears in the high side; in $\pi\pi$-mass spectra, it is on the low side. The latter case is particularly difficult for three reasons: (1) the reflection is quite close to the signal peak, (2) the reflection is rather large, and (3) the combinatorial background in this sample overall is less controlled, making a sufficiently wide fit range particularly important for accurate separation. The final choice of fit ranges for these samples are shown in Figures 5.1 and 5.2. An additional study of the sensitivity of the final measurement to the choice of the lower bound on the fit range was studied for the case of the $\pi\pi$ mass, and is reported in a later chapter.

The case of the CF samples was simpler. The only considerations were that the range be suitably balanced to facilitate at once enough width for good category separation and not so much width that background fluctuations or structure would become problematic. Since ratios are taken between the samples with and without the π_s tag, we chose the same fit range for both cases. The final choice of fit ranges for these samples are shown in Figures 5.3 and 5.4.

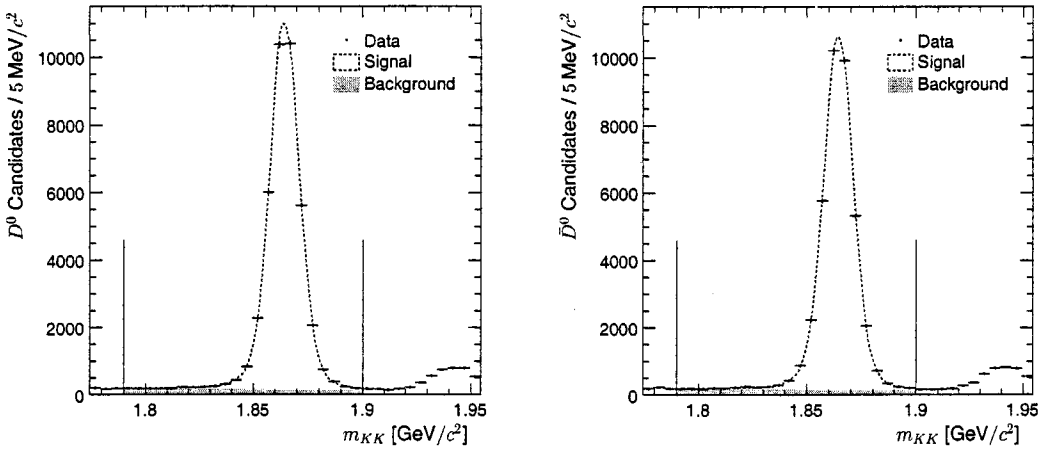

Figure 5.1: D^0-mass spectra in KK sample. Left: the KK final state reconstructed (with flavor tag) as D^0. Right: the KK final state reconstructed (with flavor tag) as $\overline{D}^0$. The two subsamples are fit simultaneously and are not efficiency-corrected.

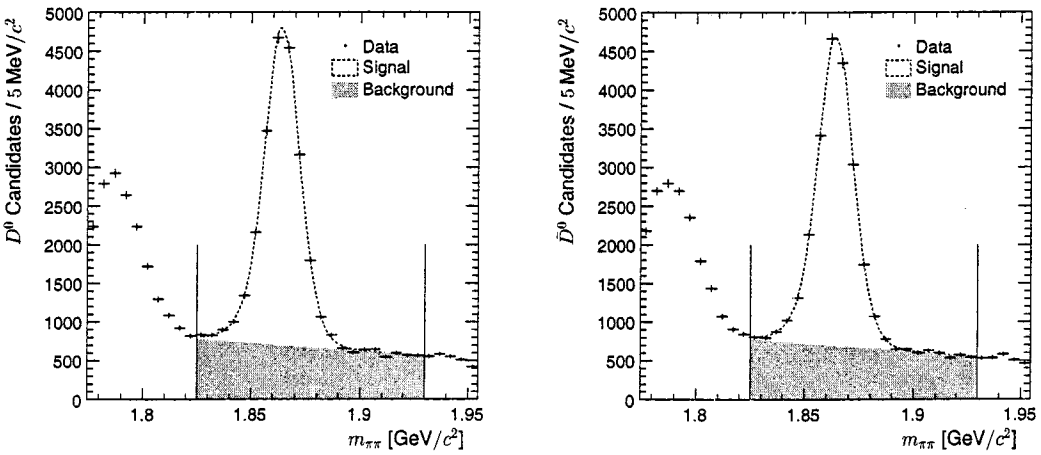

Figure 5.2: D^0-mass spectra in $\pi\pi$ sample. Left: the $\pi\pi$ final state reconstructed (with flavor tag) as D^0. Right: the $\pi\pi$ final state reconstructed (with flavor tag) as $\overline{D}^0$. The two subsamples are fit simultaneously and are not efficiency-corrected.

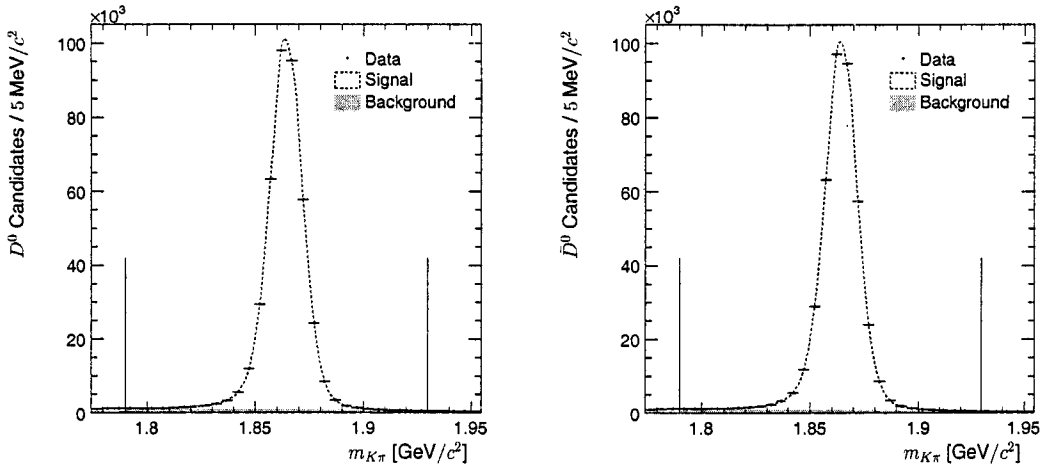

Figure 5.3: D^0-mass spectra in $K\pi$ sample. Left: the $K\pi$ final state reconstructed (with flavor tag) as D^0. Right: the $K\pi$ final state reconstructed (with flavor tag) as $\overline{D}^0$. The two subsamples are fit simultaneously and are not efficiency-corrected.

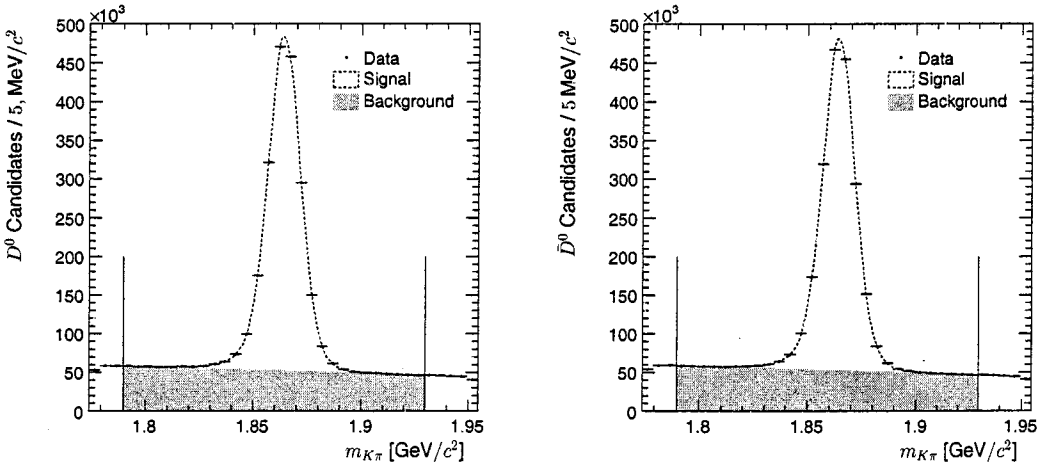

Figure 5.4: D^0-mass spectra in $K\pi$ sample (no π_s tag). Left: the $K\pi$ final state reconstructed (without flavor tag) as D^0. Right: the $K\pi$ final state reconstructed (without flavor tag) as $\overline{D}^0$. The two subsamples are fit simultaneously and are not efficiency-corrected.

5.4 Notes on Analysis Software

The optimization of fits presented here was performed using the `MINUIT` software package, supported by a custom *BABAR* package called `SlmPdfBuilder`. `SlmPdfBuilder` provides a library for use with the `ROOT` analysis program.

5.5 Fit Results

The results of these fits are shown in detail in Figures 5.5–5.8. Below each is the pull distribution used to assess the quality of the fits. For the samples that have at least one final state kaon and use flavor tagging from parent D^* reconstruction, the backgrounds are relatively low. The backgrounds in the $\pi\pi$ sample and the control $K\pi$ sample that does not use this tagging strategy are very high, and it is reasonable to ask about the precision which which we are able to discriminate our signals in these cases. To validate the fit method for use in this analysis, we approached this issue from two directions.

First, we considered the question of precise identification of signal in the presence of high combinatorial backgrounds. We performed the fit on a sample of Monte Carlo simulated data, for which we had information about the true category to which candidates belonged. This method has the following limitations. First and most important, the PID efficiencies and thus the relative background heights are known to

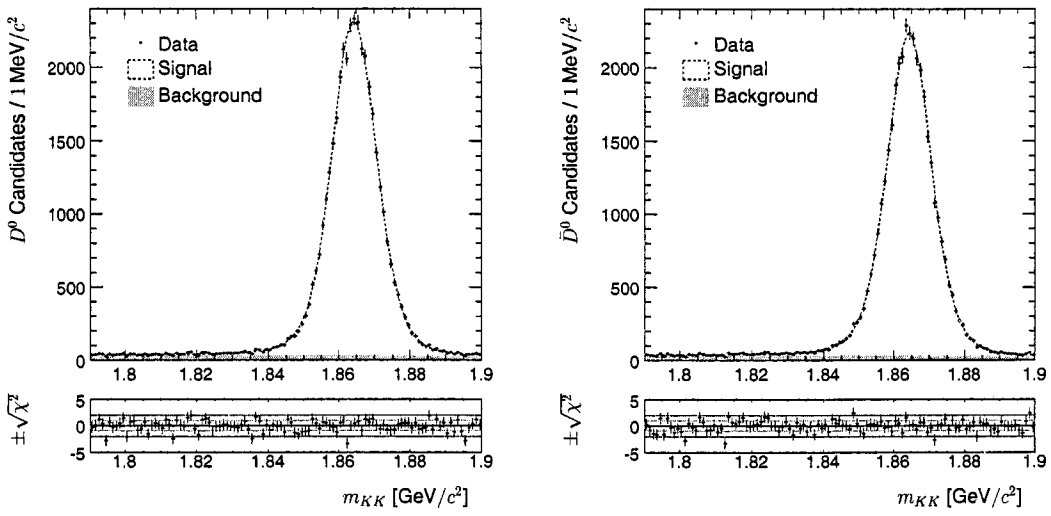

Figure 5.5: Fit to KK sample with pulls. Left: the KK final state reconstructed (with flavor tag) as D^0. Right: the KK final state reconstructed (with flavor tag) as $\overline{D}^0$. The two subsamples are fit simultaneously and are not efficiency-corrected.

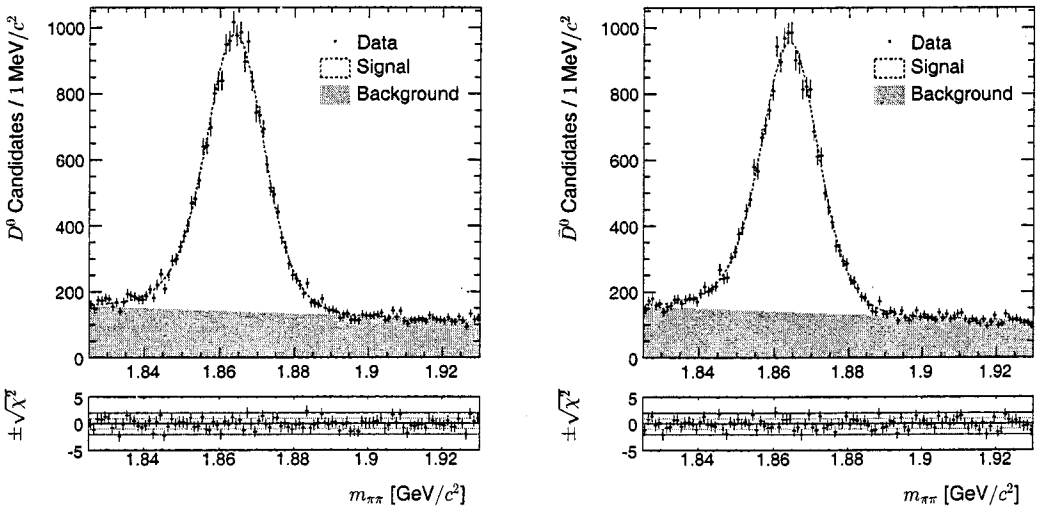

Figure 5.6: Fit to $\pi\pi$ sample with pulls. Left: the $\pi\pi$ final state reconstructed (with flavor tag) as D^0. Right: the $\pi\pi$ final state reconstructed (with flavor tag) as $\overline{D}^0$. The two subsamples are fit simultaneously and are not efficiency-corrected.

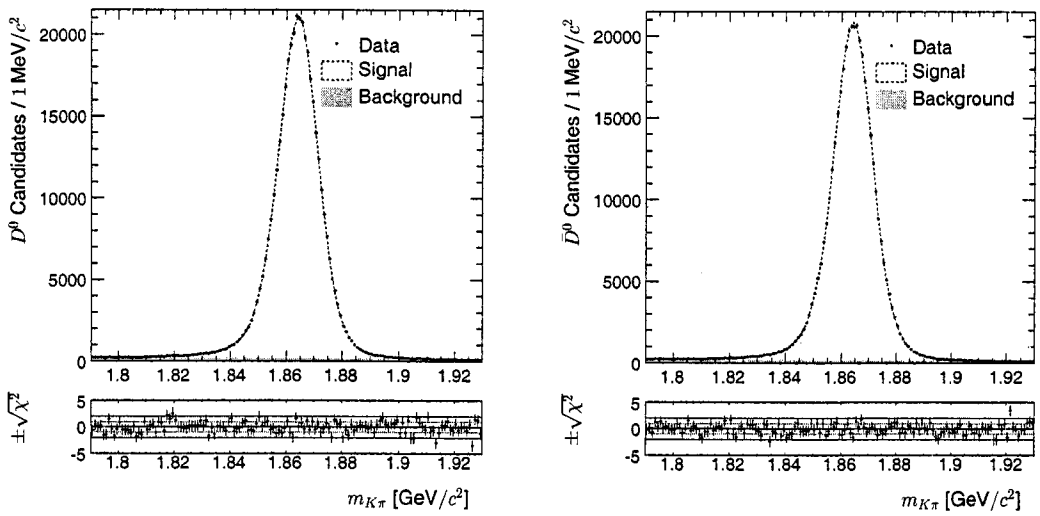

Figure 5.7: Fit to $K\pi$ sample with pulls. Left: the $K\pi$ final state reconstructed (with flavor tag) as D^0. Right: the $K\pi$ final state reconstructed (with flavor tag) as $\overline{D}^0$. The two subsamples are fit simultaneously and are not efficiency-corrected.

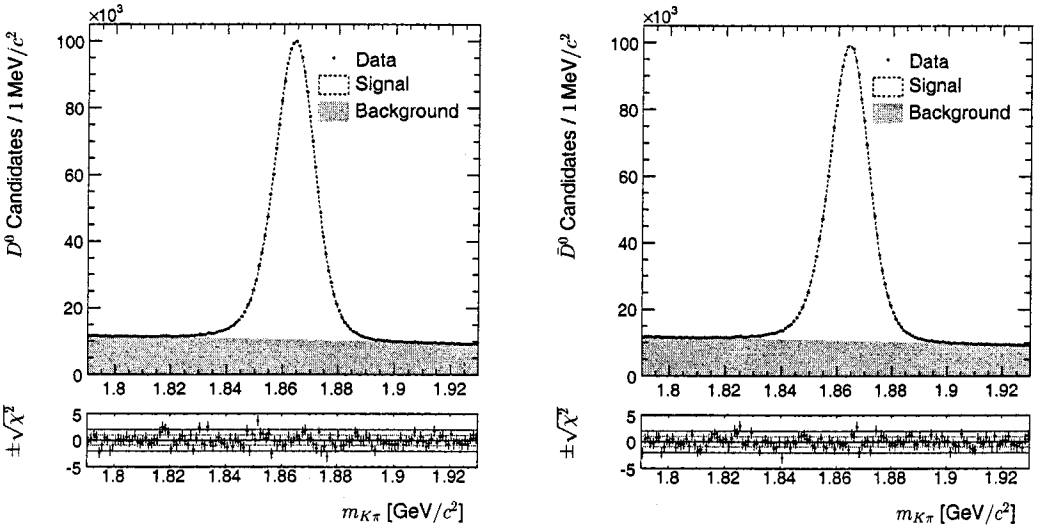

Figure 5.8: Fit to $K\pi$ sample (no π_s tag) with pulls. Left: the $K\pi$ final state reconstructed (without flavor tag) as D^0. Right: the $K\pi$ final state reconstructed (without flavor tag) as $\overline{D}^0$. The two subsamples are fit simultaneously and are not efficiency-corrected.

be imperfectly modelled in the simulated data. This is not a negligible effect, though presumably it is less relevant here since we are not actually relying on detailed shape agreement. Rather, we are concerned primarily with qualitative features of the shapes. Second, the matching between the reconstructed candidates and the truth input to the generation of the data is not perfect. This was clearly seen by inspection of distribution of candidates called false; in each case there was a visible population of signal candidates.

The fit was performed on the MC samples, and the signal yields were compared with the number of candidates known to be true D^0 or $\overline{D}^0$. Although the precise numbers were not in perfect agreement, we found excellent agreement in the relative quantities of D^0 and $\overline{D}^0$ between the two cases.

Second, we attempted to determine the sensitivity of the measured quantities to the specifics of the fit results. We did this by performing the calculations in a variety of ways. This is discussed in more detail in a later chapter. Our conclusion was the same here as above: we found that imprecision in the yields was correlated between the two flavors in a way that consistently cancelled the effect in the final results. We concluded that this fit method is adequately suited to its use in this analysis. For completeness, we performed these checks on all the samples used, and found that the accuracy of the relative yields was consistent among the samples.

The category yields for the four samples are presented in Tables 5.1 and 5.2. These

Table 5.1: Signal yields from the maximum likelihood fits to D^0 mass. Errors are statistical errors calculated directly from the fit. No corrections of any kind have been applied.

Sample	**D^0 Cand.**			**$\overline{D}^0$ Cand.**		
KK	38 760	$\pm$	290	37 470	$\pm$	260
$\pi\pi$	17 440	$\pm$	320	16 990	$\pm$	310
$K\pi$	400 570	$\pm$	910	397 810	$\pm$	900
$K\pi$ (no tag)	1 705 100	$\pm$	1 900	1 690 700	$\pm$	1 900

Table 5.2: Background yields from the maximum likelihood fits to D^0 mass. Errors are statistical errors calculated directly from the fit. No corrections of any kind have been applied.

Sample	**D^0 Cand.**			**$\overline{D}^0$ Cand.**		
KK	3 540	$\pm$	230	3 580	$\pm$	210
$\pi\pi$	13 960	$\pm$	320	13 820	$\pm$	310
$K\pi$	21 260	$\pm$	690	20 890	$\pm$	680
$K\pi$ (no tag)	1 460 900	$\pm$	1 900	1 477 500	$\pm$	2 000

are the yields obtained from the fits shown.

Chapter 6

The Soft-Pion Tagging Efficiency

6.1 Characterizing the Soft-Pion Efficiency Using Data

Measuring a_{CP} requires an understanding of our detection efficiency, since what we see in our detector will be, to use the kaon case as an example,

$$\frac{\epsilon\,\Gamma(D^0 \to K^-K^+)}{\bar{\epsilon}\,\Gamma(\bar{D}^0 \to K^+K^-)},$$

where ϵ and $\bar{\epsilon}$ are the efficiencies with which we are able to observe the particular processes. Since the final states we are interested in are shared by the numerator and the denominator, efficiencies associated with acceptance, particle identification and such will cancel by inspection. Our concern, then, must be with the efficiency of our

flavor tag:

$$\epsilon^{\pm} = \frac{\Gamma^{\rm obs}(D^{*\pm} \to \pi_s^{\pm} D^0)}{\Gamma(D^{*\pm} \to \pi_s^{\pm} D^0)}, \tag{6.1}$$

where, in this section, D^0 is used to denote a neutral charmed meson of either flavor.

As mentioned in the previous chapter on analysis strategy, we need a very precise method for evaluating the π_s efficiency for our samples. Since we can't rely on the precision of simulated data to this degree, we must determine this function from the data itself. We have chosen to do this using the Cabibbo-favored (CF) mode for two-body neutral-D decay:

$$D^0 \to K^-\pi^+.$$

This has several advantages: the CF mode does not have the charm-flavor ambiguity of the CS modes; also, since it is a two-body mode, we expect momentum spectra to behave in well-understood ways that may, with care, be applied to the CS samples.

Studies devoted to this mode generally exploit the π_s tag, but as a means of improving statistical sensitivity, not a CP discriminator. The efficiency of this tag can thus be studied by selecting a sample of neutral Ds by reconstructing this final state, and then analyzing how often they are selected by the tag. To the extent that the sample of Ds used is spectrally similar to the samples in the CS final states, this efficiency may be applied directly. Should this turn out not to the the case, some cuts and corrections may be needed to ensure applicability and accuracy.

6.1.1 The Procedure

The core idea is that we are to take a ratio between a subsample (in this case candidates with a π_s tag, denoted by $K\pi \otimes \pi_s$) and the sample from which they are drawn (denoted by $K\pi$).

Mathematically, the procedure we propose leads to the following expression of the π_s efficiency:

$$\epsilon^{\pm}(p^{\text{lab}}_{\pi_s}) = \int dp^{\text{CMS}}_{D^0} \frac{N^{\pm}_{K\pi\otimes\pi_s}(p^{\text{CMS}}_{D^0}, p^{\text{lab}}_{\pi_s})}{N^{\pm}_{K\pi}(p^{\text{CMS}}_{D^0})}. \tag{6.2}$$

This rather cumbersome equation breaks down in the following way. Our goal is to produce the flavor-tagging efficiency as a function of the momentum of the soft pion. This momentum is measured in the rest frame of the laboratory (p^{lab}). Due to the physics of charged particle detection, it is expected that this is a coordinate for observing a charge-asymmetric efficiency.

Once we have determined the final form we will use, we must decide on a procedure for weighting the number of tagged candidates by the number of candidates in the sample for which no tag has been calculated. The simplest way would simply be to take the bulk ratio. However, since we do not know *a priori* whether the tag preserves the the spectral shape, this is not a cautious choice. We have chosen to perform our calculation in bins of D^0 momentum, and then project back to the final form described above. This is represented in the expression by the integral. The D^0

momentum is expressed in the center-of-mass rest frame ($p^{\rm CMS}$) because this is the frame in which we have made a cut on this momentum to eliminate background from B decays, as discussed in Chapter 4. In summary, our procedure is to take the ratio of the two D^0-momentum spectra (tagged to no-tag) in bins of π_s momentum.

6.2 Validation of Calculation Method

The decay dynamics of the samples in the different two-body modes of the D^0 appear to be similar enough for our purposes, as is illustrated in the momentum and angular spectra of Ds (Figures 6.1 and 6.2), reconstructed in the different final states. What is also clear, however, is that the different particle-identification efficiencies for kaons and pions contributes to significantly different attenuation in the angular distributions (see Figures 6.2). The relative behaviors, with KK and $\pi\pi$ falling on either side of $K\pi$, is to be expected. The low populations at the left side of the distributions are also somewhat undesirable, leading to the choice of a fiducial region of $|\cos\theta^{\rm lab}_{D^0}| < 0.8$ for all of our D^0 samples.

Since we are performing this calculation using histogram arithmetic, it is possible that results could be sensitive to bin widths. This would indicate that the binned distributions were an insufficient approximation to their unbinned counterparts. In this procedure, the variation of the asymmetry over the independent variable chosen, p_{π_s} reflects the shape of the momentum spectrum of the neutral D. Thus, to the extent

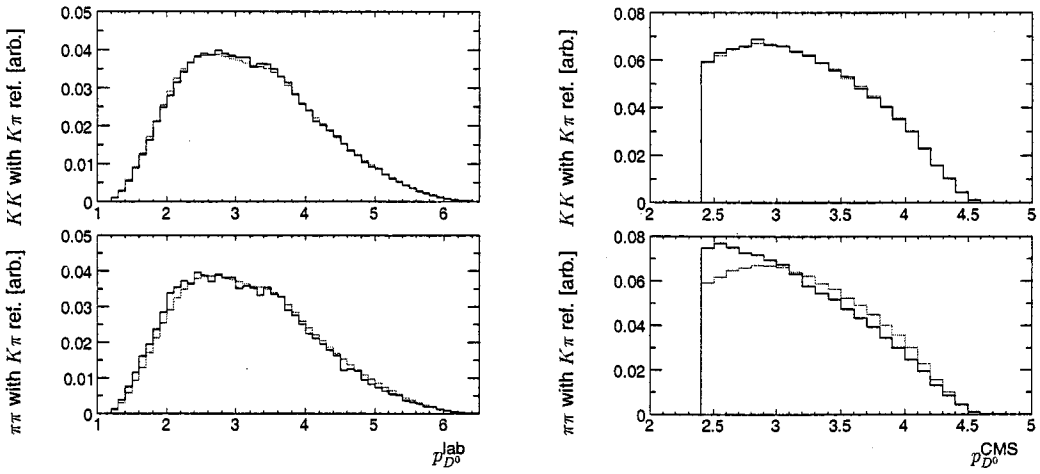

Figure 6.1: Scaled spectra of p_{D^0} for CS and CF modes. Vertical units are arbitrary due to scaling, which is used since samples sizes are different among modes. Samples combine charge conjugate states in a tight signal region, and are not yet background-subtracted. Upper: $D^0 \to KK$ (black) with $D^0 \to K\pi$ (grey) for reference. Lower: $D^0 \to \pi\pi$ (black) with $D^0 \to K\pi$ (grey) for reference.

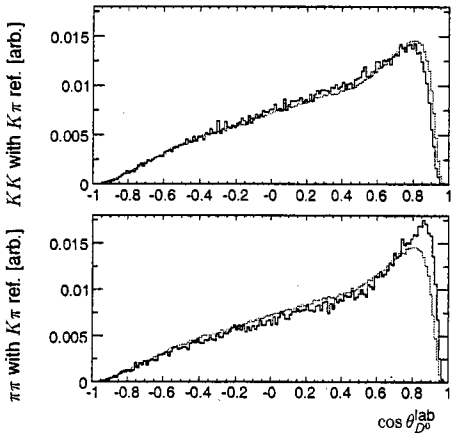

Figure 6.2: Scaled spectra of $\cos\theta_{D^0}^{\rm lab}$ for CS and CF modes. Vertical units are arbitrary due to scaling, which is used since samples sizes are different among modes. Samples combine charge conjugate states in a tight signal region, and are not yet background-subtracted. Upper: $D^0 \to KK$ (black) with $D^0 \to K\pi$ (grey) for reference. Lower: $D^0 \to \pi\pi$ (black) with $D^0 \to K\pi$ (grey) for reference.

that this distribution may be distorted by binning, the result could be dependent on bin choices. We found that there was a minimum number of bins required to capture the shape of this distribution (about 5), and above that the result was insensitive to binning.

We considered fitting the resulting efficiency as a function of π_s momentum before applying it to the background-subtracted CS samples. We found that the result was very robust with respect to bin width. Introducing another fit seemed unlikely to reduce overall uncertainty in this case, and consequently it was decided against.

6.3 The Statistical Background-Subtraction Method

All background subtraction in this analysis is performed using a statistical event-weighting method [5]. Weights are calculated from the likelihood fit, and may be both positive and negative. All events are weighted, and the resultant distribution of weights is commonly called the signal distribution, though here we choose to describe it as a background-subtracted distribution. The procedure is described in some generality below. Ours is the simple case of only two categories.

Each candidate is assigned a signal weight calculated from the results of the ML fit:

$$w_{sig}(\vec{q}_k) = \frac{\sum_{j=1}^{n} V_{sig,j} P_j(\vec{q}_k)}{\sum_{j=1}^{n} N_j P_j(\vec{q}_k)}, \tag{6.3}$$

where j spans signal ($j = sig = 1$) and background ($j = 2, ..., n$) PDFs, $\vec{q}_k$ is the vector of dependent-variable values (in our case, the single-element m^{reco}) for the k^{th} candidate, $P_j(\vec{q}_k)$ is the value of the j^{th} PDF evaluated for the k^{th} candidate, N_j is the j^{th} category yield, and $V_{sig,j}$ are the covariance matrix elements of the parameters N_{sig} and N_j. The covariance matrix V_{ij} is not the full covariance matrix from the maximum likelihood fit, but rather the sub-matrix for the category-yields parameters only, given by

$$V_{ij}^{-1} = \sum_k \frac{P_i(\vec{q}_k)P_j(\vec{q}_k)}{(\sum_{l=1}^{n} N_l P_l(\vec{q}_k))^2}. \tag{6.4}$$

These signal weights quantify the statistical separation of signal from background determined by the maximum likelihood fit, and they have the property that

$$\sum_k w_{sig}(\vec{q}_k) = N_{sig}. \tag{6.5}$$

The reason for using this scheme for the background subtraction is that, as in the case of sideband subtraction techniques, events likely to fall in the the background category may be identified in one distribution (say, mass) and then subtracted in another (say, momentum). We would like the full statistical advantage of a fit, but if we could use only the resultant functional descriptions of the signal and background categories, we would be unable to distinguish between the categories on an event-by-event basis, as is needed to separate the categories in distributions not included in the fit.

6.4 Estimate of Statistical Uncertainty

The statistical uncertainty on this measurement is due to the uncertainty of the yields from which it is calculated. These are reported in Table 5.1. Calculation of the exact uncertainty is significantly complicated by the combination of two factors. First, the two samples are clearly correlated, since one is a subsample of the other. Second, the final result is a non-trivial construct of the raw distributions. Thus to propagate the errors exactly becomes quite difficult. Instead, we attempt to estimate the scale of the expected errors considering sample correlations, and combine this with the behavior obtained from a simple uncorrelated calculation of the errors based on the histogram arithmetic used in the calculation.

6.4.1 Error from Correlation of Samples

At zeroth order, the efficiency we calculate is a simple ratio of yields, $\epsilon_0 = N_{K\pi\otimes\pi_s}/N_{K\pi}$. This is what we would have if we were to ignore the possibility of different spectral shapes through out the analysis. Thus the yields would not be binned into histograms, and the efficiency would have this very simple form.

To calculate the error on this simple efficiency we must not forget that $N_{K\pi\otimes\pi_s}$ is a subset of $N_{K\pi}$. We can account for this by performing the calculation in an

Table 6.1: ϵ_0 and σ_ϵ for the two flavor cases.

	ϵ_0	σ_ϵ
ϵ_0^+	0.2349	0.0005
ϵ_0^-	0.2353	0.0005
ϵ_0^r	0.998	0.003

uncorrelated coordinate system by observing that we can define

$$N_a = N_{K\pi\otimes\pi_s},\ N_b = N_{K\pi} - N_{K\pi\otimes\pi_s}.$$

The variables N_a and N_b are clearly uncorrelated. We perform the error calculation and transform back to the coordinates of interest.

By this procedure, we obtain this expression for the uncertainty of the efficiency:

$$\sigma_\epsilon^2 = (\frac{N_\otimes - N}{N^2})^2\sigma_{N_\otimes}^2 + \frac{N_\otimes^2}{N^4}(\sigma_N^2 - \sigma_{N_\otimes}^2) \tag{6.6}$$

in which the shortened $N_\otimes$ and N have been used for $N_{K\pi\otimes\pi_s}$ and $N_{K\pi}$ respectively. Values are presented in Table 6.1.

6.4.2 Dependence of Error on π_s Momentum

Since we actually use the the more complex version of the efficiency described earlier, which is a function the soft-pion momentum p_s^{lab}, we would like to estimate how the error might vary as a function of this variable as well. We also expect that the statistical power of the sample must be reduced by the binning procedure, so we use

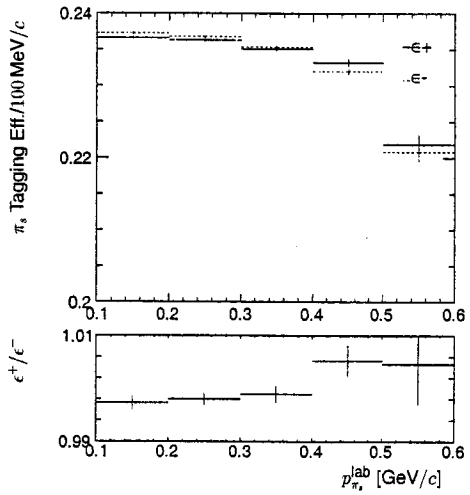

Figure 6.3: π_s tagging efficiency; D^0 (solid), $\overline{D}^0$ (dashed). The ratio of the two is shown in the lower plot. The samples are background-subtracted using a statistical event-weighting procedure (called *sPlots* in the literature).

the following estimate for the error of one bin, ϵ_i, of the efficiency:

$$(\sigma_\epsilon)_i = \sqrt{\frac{N_\otimes}{(N_\otimes)_i}}\,\sigma_\epsilon. \tag{6.7}$$

6.5 Results

We find that the overall charge asymmetry in detection of soft pions in *BABAR* is actually quite small. These results are shown in Figure 6.3 and summarized in Table 6.2. This is a satisfying result, in that it suggests that *BABAR* provides a good laboratory for a precision measurement of the kind we are attempting.

Table 6.2: Overall tag asymmetry in bins of π_s momentum, with errors.

$p_{\pi_s}^{\mathrm{lab}}$ [MeV/c]	ϵ_i^+	ϵ_i^-	ϵ_i^r
100–200	0.23659 ± 0.00020	0.23723 ± 0.00021	0.9973 ± 0.0012
200–300	0.23629 ± 0.00018	0.23677 ± 0.00018	0.9980 ± 0.0011
300–400	0.23509 ± 0.00026	0.23534 ± 0.00025	0.9989 ± 0.0015
400–500	0.23321 ± 0.00049	0.23199 ± 0.00047	1.0052 ± 0.0029
500–600	0.22186 ± 0.00129	0.22085 ± 0.00124	1.0046 ± 0.0076

Chapter 7

Systematic Studies and Checks

7.1 Systematic Studies of the Mass Fit

7.1.1 Perturbation of the PDF Shape

To quantify possible systematic uncertainty introduced by our choice of PDF shape in the D^0 mass fit, we make a change to the model used, and look at the resultant change in yields. This is done by adding a second-order contribution to the background shape. This is designed to allow to the background distribution the possibility of consuming a portion of the signal, or rejecting a portion of the background, through the introduction of curvature in the distribution. We will then quantify the effect that this has on the flavor ratios to investigate whether it could be a source of artificial asymmetry.

Table 7.1: Flavor ratios with perturbed PDF shapes.For each sample, the ratio of signal yields for D^0 to $\overline{D}^0$ are given with (Perturb.) and without (original) the additional of a quadratic background-shape term.

Sample	Perturb.	Original
KK	1.036 ± 0.008	1.035 ± 0.008
$\pi\pi$	1.032 ± 0.015	1.027 ± 0.012
$K\pi$	1.005 ± 0.002	1.007 ± 0.002
$K\pi$ (no tag)	1.009 ± 0.001	1.009 ± 0.001

The results of this study are presented in Table 7.1. In the case of each sample, adding a quadratic term to the background model did not significantly alter the flavor ratios measured. The table compares the results with those of the fits used in this analysis.

7.1.2 The $\pi\pi$ Fit Range

A special procedure was used to validate the choice of fit range for the $\pi\pi$ sample, due to concern about the proximity of the $K\pi$ reflection to the signal peak. The low-mass cutoff was originally selected by inspection, but since the separation between the peaks is somewhat poor, we decided to scan the vicinity and determine the robustness of the flavor ratio with respect the the choice of value for this cutoff. The results of this scan are shown in Table 7.2.

For the full scan range presented, the fits were mathematically well-behaved; they

Table 7.2: Dependence of fitted $\pi\pi$ flavor ratio on fit range. The first column (Cutoff) is the value chosen for the low end of the fitted interval. The second column (Flavor Ratio) is the ratio of fitted signal yields for D^0 to $\overline{D}^0$, with errors from the covariance matrix obtained from the fit. The value in bold has been selected for this analysis.

Cutoff (GeV)	**Flavor Ratio**
1.810	1.027 ± 0.013
1.815	1.026 ± 0.014
1.820	1.027 ± 0.014
1.825	$\mathbf{1.027 \pm 0.012}$
1.830	1.028 ± 0.013
1.835	1.028 ± 0.013
1.840	1.036 ± 0.018
1.845	1.038 ± 0.018

were convergent and errors were estimated by MINUIT. However, at either end of the range there were observable qualitative reasons to reject the quality of the fit. At the low end, we stopped the scan at 1.810 GeV because although the fit converged, it no longer met the basic goodness-of-fit criteria outlined in the chapter dedicated to the fit procedure. There was very clear structure in the pull distribution, since this far into the reflection peak the linear background model was very inadequate. On the high end, we begin to visibly cut into the signal region, and we no longer have confidence in our ability to separate signal from background. This is certainly the case by the end of our range, at 1.845 GeV; in fact the change in the behavior of the flavor ratio beginning near 1.840 GeV leads us to suspect that we have inadequate sideband coverage well before the end of the scan range. Nonetheless, there is clearly a sufficient range

through which the ratio and error are robust, leading to the conclusion that we are not overly sensitive to our choice for this cutoff.

7.2 Systematic Studies of the Slow-Pion Efficiency

The most obvious source of systematically introduced flavor asymmetry is in the flavor tag itself. We study the overall sensitivity of the correction to the procedural details.

7.2.1 Study of Remaining Spectral Distortions

Uncorrected spectral distortions due to detector effects could manifest themselves through a dependence in CP asymmetries on momentum variables. We check for such a dependence in our final samples and present the results in Figures 7.1 and 7.2. There does appear to be evidence for residual uncorrected detector effects in both modes. Similar behavior is seen in simulated samples. We conclude that the tagging-efficiency procedure used is not adequate for the correction of spectral shapes, and that additional study is warranted. We estimate that the remaining systematic uncertainty on a_{CP} is 0.5%. This estimate is based on the behavior of the simulated data for which there is no CP asymmetry expected.

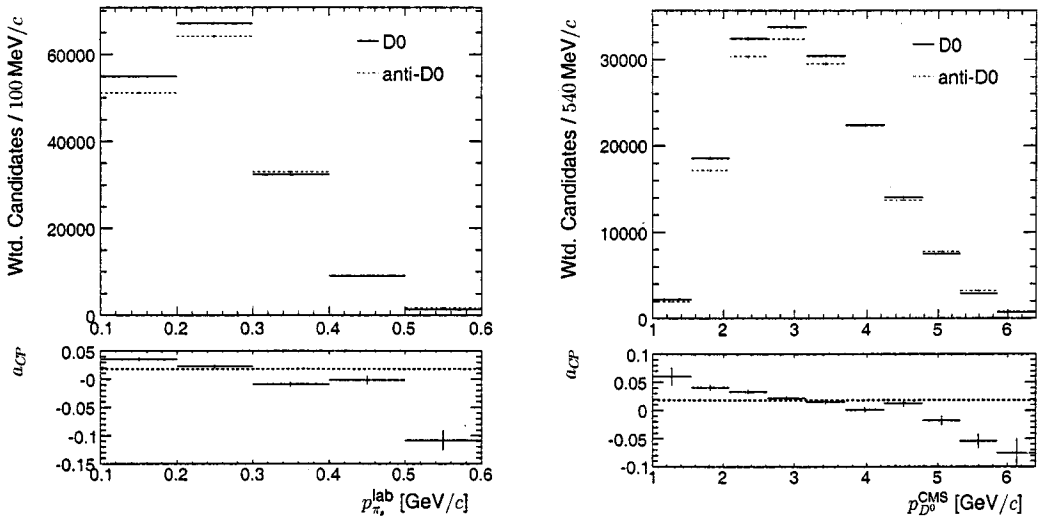

Figure 7.1: Final momentum spectra for KK samples: π_s, left; D^0, right. Below are shown a_{CP} as functions of these variables. Distributions have been background-subtracted and efficiency-corrected. Deviations in the lower plots from flatness indicate remaining systematic effects. Guidelines are drawn at centroid values.

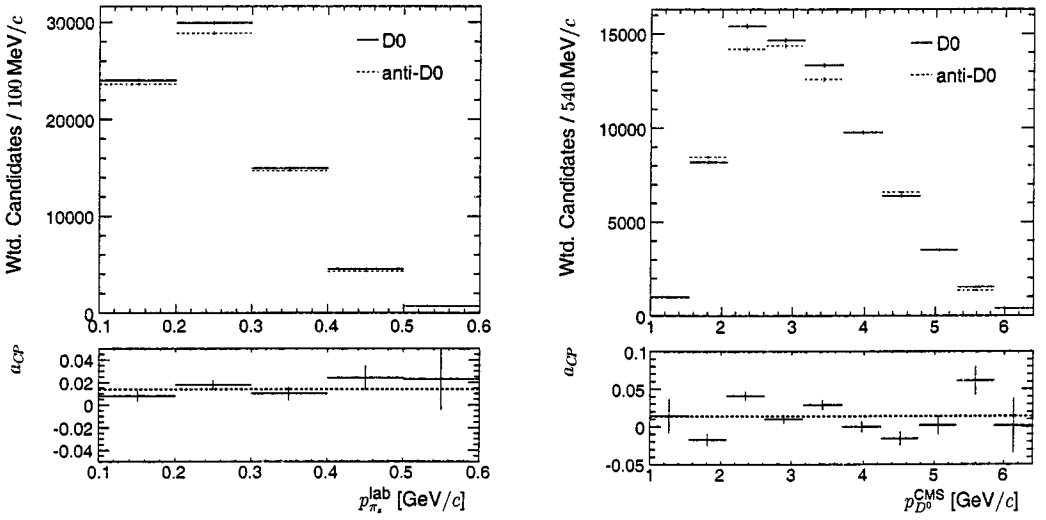

Figure 7.2: Final momentum spectra for $\pi\pi$ samples: π_s, left; D^0, right. Below are shown a_{CP} as functions of these variables. Distributions have been background-subtracted and efficiency-corrected. Deviations in the lower plots from flatness indicate remaining systematic effects. Guidelines are drawn at centroid values.

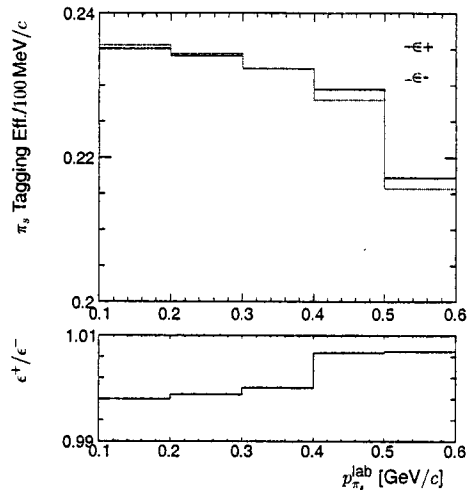

Figure 7.3: π_s tagging efficiency; D^0 (solid), $\overline{D}^0$ (dashed). The ratio of the two is shown in the lower plot. The samples are background-subtracted using a mean sideband subtraction.

7.2.2 Study of Background Subtraction Method

We begin by performing the calculation of the efficiency without using any fitting at all. Since the combinatorial background in the CF mode is free of reflections and other non-linear features, a simple mean-sideband background subtraction should be fairly accurate. We define a signal region and high and low sidebands for the sample. The efficiency correction is calculated within the signal region after a subtraction of the mean of the sidebands. (By this we indicate that each of the equal-width sidebands was weighted by half and subtracted from the signal region.) The resulting efficiency correction is given in Figure 7.3.

The efficiency calculated using this background subtraction technique looks very similar to that used in this analysis. Further, the resultant ratio for the two π_s charges

is even more similar. This indicates that the background subtraction method used in this analysis is not a significant source of systematic error.

7.2.3 Systematic Uncertainty in Fit Procedure

As described in the chapter about the fit procedure, each sample is fit for yields of D^0 and $\overline{D}^0$ simultaneously. In this fit, the signal shape is assumed to be the same for the two flavors. This is true for the CS samples; for the CF samples, there could be a slight resolution asymmetry for the two flavors due to charge asymmetry in the final state reconstruction. This effect is expected to be negligible. Additionally, there is a small known correlation between the reconstructed mass of the D^0 and the associated reconstructed $\Delta m = m_{D^*} - m_{D^0}$. Thus, it is expected that the Δm cut used in the flavor tag would have a slight narrowing effect on the D^0 mass distribution. For this reason, we chose to fit the samples with and without the tag separately. However, in the presence of the high combinatorial background found in the sample without the tag, it is conceivable that the fit might have trouble fitting the signal shape correctly.

For these reasons we perform the following systematic studies of the simultaneous fit of the CF samples. We fit the samples using the following modified procedures, and observe the comprehensive effect on the charge asymmetry of the efficiency. In the first modification, instead of fitting the tagged sample (D^0 and $\overline{D}^0$ simultaneously), and separately fitting the sample without the tag (also D^0 and $\overline{D}^0$ simultaneously), we

Table 7.3: Systematic study charge asymmetry in tag from fit method. (1) Method used in this analysis; (2) method fitting simultaneously by D^0 flavor; (3) method fitting sample without tag fixing signal shape to tagged sample.

Method	ϵ_0^+	ϵ_0^-	ϵ_0^r
(1)	0.2349 ± 0.0005	0.2353 ± 0.0005	0.998 ± 0.003
(2)	0.2327	0.2330	0.999
(3)	0.2325	0.2328	0.999

fit the two D^0 samples (with and without tag simultaneously), and separately fit the two $\overline{D}^0$ samples (also with and without tag simultaneously). In the second modified procedure, we retain original sample configuration, but we fix the signal shape of the high background (no tag) sample to that optimized in the low background (tagged) fit.

The results of the modifications are presented in Table 7.3. We quantify resultant effect on the measured charge asymmetry by considering the change to $\epsilon_0^r = \epsilon_0^+/\epsilon_0^-$. We find that the size any systematic error is insignificant compared with the statistical error.

7.3 Performing the Analysis on Simulated Data

7.3.1 The Monte Carlo Dataset

As a validation of the cumulative analysis method and implementation, the analysis was performed from beginning to end on a Monte Carlo simulated dataset. The

software implementation was not modified in any way; only the input data was different. The cumulative simulated sample is designed to mimic at least the statistical sensitivity of the experimental data (in fact it is slightly larger). It is also designed to mimic the content of the true dataset as much as possible. To this end, it is a combination of simulated B-meson decays and lighter quark-pair events (u,d,s and c) with simulated hadronization and decays. From the point of view of this analysis, the main weakness of the simulated data is that it is not able to accurately model the PID of the physical *BABAR* detector, in terms of efficiencies and misidentification rates. This means that the spectral shapes and background levels are not reliably accurate, although they are qualitatively similar to the data in general ways. Of particular difference are the charge asymmetries in combinatorial backgrounds and PID efficiencies. Thus, we do not make any direct comparisons of collected data to simulated data; rather, we use the simulated data to check the analysis method and implementation.

7.3.2 Validation of Signal Extraction from Fits

In addition to performing the D^0 mass fits to the simulated distributions, we take advantage of the known truth at generation to further validate yields from the fits. The resulting ratios of signal yields for each sample is reported here. As described in the chapter dedicated to the fits, we here exploit the the fact that we know what the generated samples were, so we can compare the ratios from the fits to the ratios from

Table 7.4: Flavor ratios in simulated data. Under the Fit heading are D^0 signal yields relative to $\overline{D}^0$, with errors calculated from the MINUIT covariance matrix. Under the MC Truth heading are the same ratios calculated directly from numbers of Mont-Carlo Truth candidates.

Sample	Fit	MC Truth
KK	1.007 ± 0.006	1.009
$\pi\pi$	1.011 ± 0.011	1.007
$K\pi$	0.989 ± 0.002	0.989
$K\pi$ (no tag)	0.988 ± 0.001	0.987

the truth-matching of the candidates. The results are presented in Table 7.4.

Since the simulated is known to have resolutions, background shapes, *et cetera*, that deviate from those in the data from the physical detector, we perform a scan of the low-mass cutoff in the simulated $\pi\pi$ sample. The results of this scan are included for completeness in Table 7.5

As discussed above in the description of this scan for data, at either end of the range we have clear reasons to distrust the fit; nonetheless, we look for a stable intermediate range. As in the case described above, we are able to validate the value selected by inspection of the distribution.

7.3.3 Results

The results for the quantities calculated in this analysis using simulated Monte Carlo data are presented in the Table 7.6. They are consistent with no *CP* asymmetry,

Table 7.5: Dependence of fitted $\pi\pi$ flavor ratio on fit range in simulated data. The first column (Cutoff) is the value chosen for the low end of the fitted interval. The second column (Flavor Ratio) is the ratio of fitted signal yields for D^0 to $\overline{D}^0$, with errors from the covariance matrix obtained from the fit. The value in bold has been selected for this analysis.

Cutoff (GeV)	**Flavor Ratio**
1.825	1.018 ± 0.011
1.830	1.011 ± 0.013
1.835	$\mathbf{1.011 \pm 0.011}$
1.840	1.005 ± 0.013
1.845	1.018 ± 0.004

Table 7.6: *CP* asymmetry results for simulated data. Uncertainties are statistical only.

Mode	a_{CP}
KK	$(0.2 \pm 0.3)\%$
$\pi\pi$	$(0.5 \pm 0.6)\%$
R	$(-0.3 \pm 0.7)\%$

at the level of the statistical sensitivity of the sample. However, we note that in both modes, the result was high. This could be accidental, but it also could be related to the spectral distortions above. Should a larger sample of simulated data be available, it would be able to distinguish between these different affects.

Chapter 8

Results and Conclusions

8.1 Results

8.1.1 a_{CP} in Each Mode

We present our results for Direct CP violation in each of the two-body CS channels for neutral D decay in Table 8.1. The statistical error given is due to the statistical error on the fitted yields; the efficiency correction was found to have an insignificant contribution. Based on the systematic studies we performed and presented, we have included a systematic uncertainty that is the quadrature sum of the two dominant sources discussed in Chapter 7. The larger is that due to residual spectral distortions (0.5%). In addition, there is a contribution estimated to be the difference in the results we would have seen had we used the perturbed PDF instead of that chosen for this

Table 8.1: CP asymmetry results. The first uncertainty in each case statistical and the second systematic.

Mode	a_{CP}
KK	$(1.8 \pm 0.4 \pm 0.5)\%$
$\pi\pi$	$(1.4 \pm 0.6 \pm 0.6)\%$
R	$(0.4 \pm 0.7 \pm 0.8)\%$

analysis. All other sources of uncertainty considered were relatively insignificant.

As shown in the table, our statistical sensitivity in the KK mode is much better than that in the $\pi\pi$ mode, due to their relative branching fractions. Unfortunately, these results are systematically limited at this time.

8.1.2 Asymmetry of the Branching Ratio

Our observation of the CP asymmetry of the branching fraction is also given in Table 8.1. Although presented only once, this quantity was calculated in three different ways; each method gave the same result.

First, this quantity and its errors were calculated from the final (corrected) yields. As a cross-check, they were then calculated from the uncorrected yields, since the correction cancels in this construction. Finally, they were calculated directly from the difference between the asymmetry in each mode individually.

8.2 Conclusions

The results of this analysis are very interesting in the the context of the Standard Model and previous experimental results. Our results are shown in the context of previous published searches in Figures 8.1 and 8.2. Despite the systematic limitation of these results, this analysis strategy is already able to produce an improvement to the world average. However, the statistical power of the samples is a strong motivation for improvement to the method. We believe that with additional study, systematic effects can be understood to the level of $\mathcal{O}(10^{-3})$. Nevertheless, these results, particularly for the KK mode, are suggestive of a level of CP violation that cannot be accounted for within the Standard Model.

The charm-flavor sector of experimental particle physics has much yet to be measured and understood, but could prove to be a source of very interesting new results in the near future.

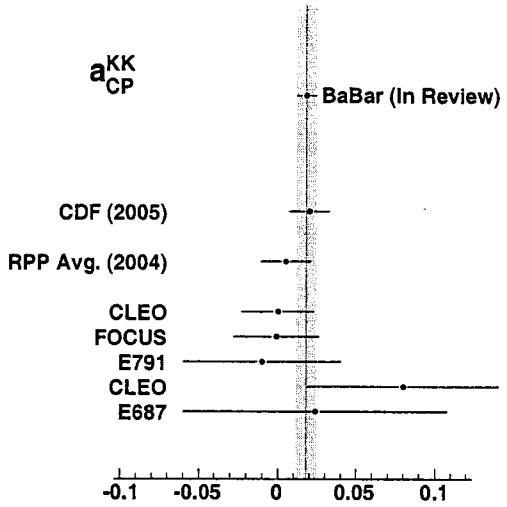

Figure 8.1: World results for a_{CP}^{KK}. At top (and bar) are the results of this work for comparison. Listed below with years are the recent CDF result (2005) and the most recent world average calculated by the the Particle Data Group (2004). Below this are the individual results included in the 2004 world average.

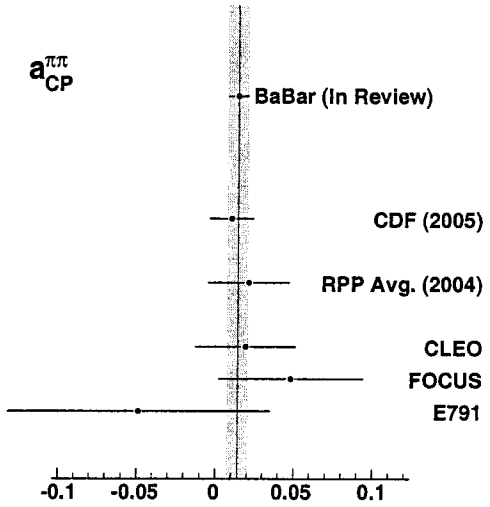

Figure 8.2: World results for $a_{CP}^{\pi\pi}$. At top (and bar) are the results of this work for comparison. Listed below with years are the recent CDF result (2005) and the most recent world average calculated by the the Particle Data Group (2004). Below this are the individual results included in the 2004 world average.

Appendix A

Standard Candidate Lists

A.1 General Track Lists

A.1.1 `GoodTracksVeryLoose`

- $d_{xy} < 1.5\,\text{cm}$, where d_{xy} is the distance of closest approach (DOCA) to the beamspot in the transverse plane (relative to the beam axis)
- $d_z < 10\,\text{cm}$, where d_z is the DOCA to the beamspot along the direction of the beam axis

A.1.2 `GoodTracksLoose`

- $d_{xy} < 1.5\,\text{cm}$, where d_{xy} is the distance of closest approach (DOCA) to the beamspot in the transverse plane (relative to the beam axis)
- $d_z < 10\,\text{cm}$, where d_z is the DOCA to the beamspot along the direction of the beam axis
- $p_t > 100\,\text{MeV}/c$, where p_t is the transverse lab-momentum relative to the beam axis
- At least 12 hits in the drift chamber

A.2 Particle Identification Lists

A.2.1 `KLHTight`

For each track, the selector calculates likelihoods $\mathcal{L}$ for several particle hypotheses. The particle types checked are K, π, p, μ, and e. The likelihood calculations use information from the SVT and DCH, such as dE/dx and number of hits; information from the EMC, such as E/P; and information from the DRC, such as the Cerenkov angle and the number of photons. The selector combines the likelihoods into ratios, and make cuts to select tracks with a given efficiency and fake rate.

Histograms showing the various efficiencies of this selector are found in Figures A.1–A.6.

A.2.2 KLHVeryTight

This selector calculate likelihoods as for the KLHTight selector described above, making different cuts on the ratios.

Histograms showing the various efficiencies of this selector are found in Figures A.7–A.12.

A.2.3 piLHTight

This selector calculate likelihoods as for the KLHTight selector described above, making different cuts on the ratios.

Histograms showing the various efficiencies of this selector are found in Figures A.13–A.18.

A.2.4 piLHVeryTight

This selector calculate likelihoods as for the KLHTight selector described above, making different cuts on the ratios.

Histograms showing the various efficiencies of this selector are found in Figures A.19–A.24.

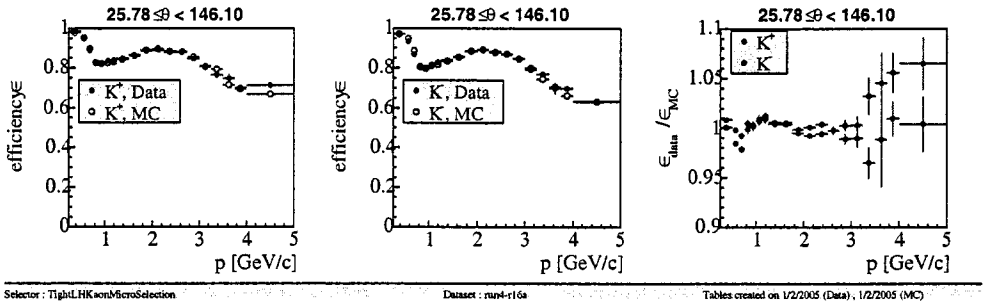

Figure A.1: Efficiencies for selecting $K^{\pm}$s using the `KLHTight` list in Monte Carlo and data. The histograms show the efficiency as a function of momentum for the entire detector acceptance range. The left shows the efficiency for selecting K^{+}, the center shows the efficiency for selecting K^{-}, and the right shows the ratio of efficiency in data to that in Monte Carlo.

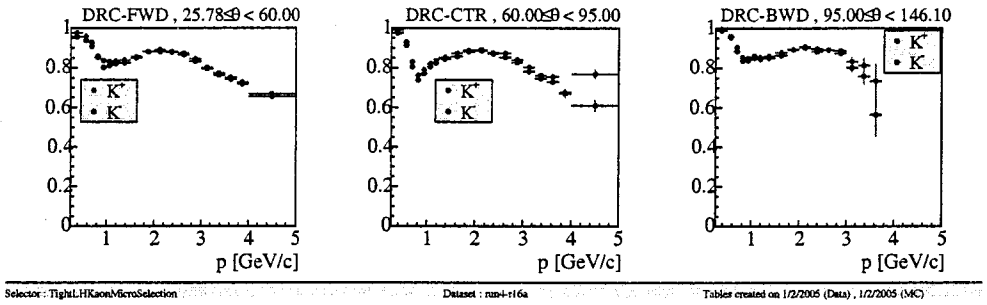

Figure A.2: Efficiencies for selecting $K^{\pm}$s using the `KLHTight` list in data. The histograms show the efficiency for K^{-} and K^{+} as a function of momentum for the forward section of the detector (left), the center section (center), and the backward section (right)

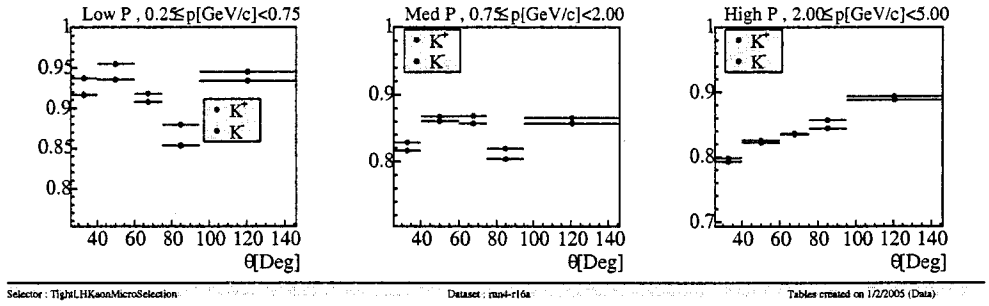

Figure A.3: Efficiencies for selecting $K^{\pm}$s using the `KLHTight` list in data. The histograms show the efficiency for K^- and K^+ as a function of polar angle for the low-momentum tracks (left), medium-momentum tracks (center), and high-momentum tracks (right)

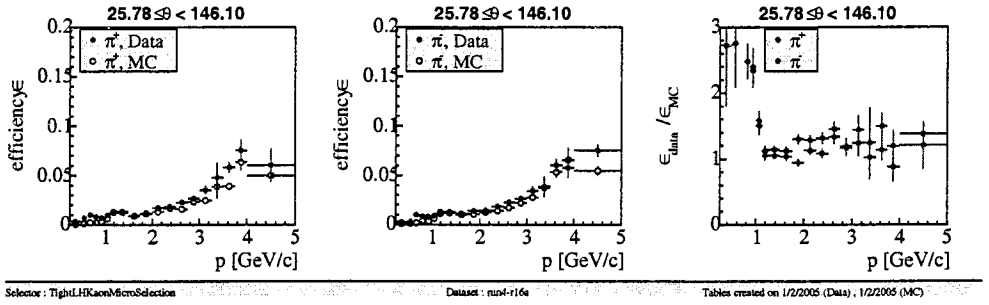

Figure A.4: Efficiencies for selecting $\pi^{\pm}$s using the `KLHTight` list in Monte Carlo and data. The histograms show the efficiency as a function of momentum for the entire detector acceptance range. The left shows the efficiency for selecting π^+, the center shows the efficiency for selecting π^-, and the right shows the ratio of efficiency in data to that in Monte Carlo.

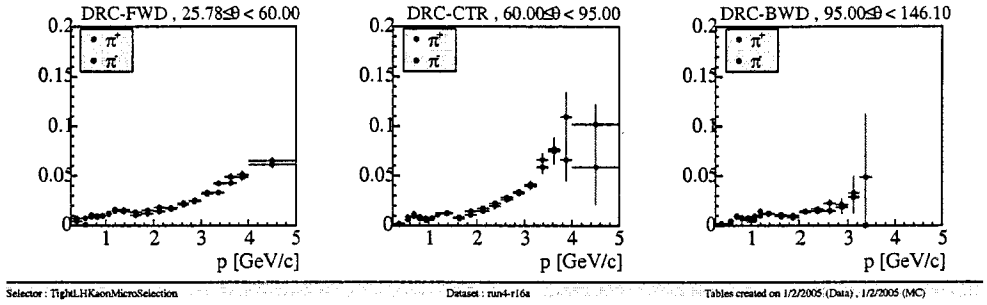

Figure A.5: Efficiencies for selecting $\pi^{\pm}$s using the `KLHTight` list in data. The histograms show the efficiency for π^- and π^+ as a function of momentum for the forward section of the detector (left), the center section (center), and the backward section (right)

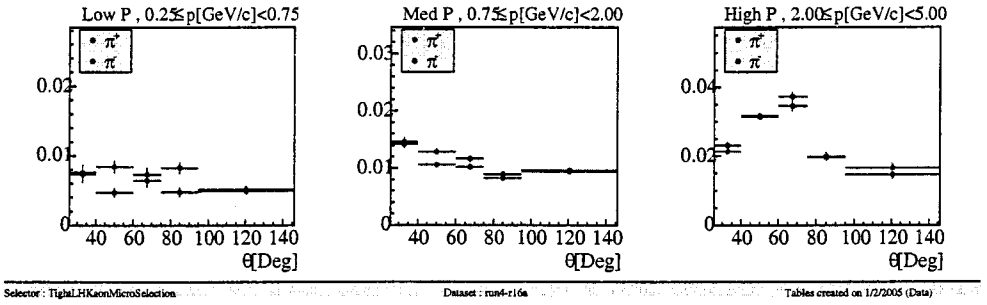

Figure A.6: Efficiencies for selecting $\pi^{\pm}$s using the `KLHTight` list in data. The histograms show the efficiency for π^- and π^+ as a function of polar angle for the low-momentum tracks (left), medium-momentum tracks (center), and high-momentum tracks (right)

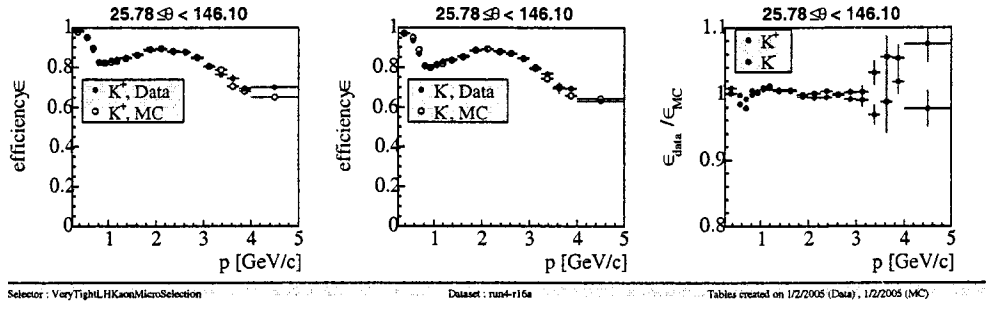

Figure A.7: Efficiencies for selecting $K^{\pm}$s using the `KLHVeryTight` list in Monte Carlo and data. The histograms show the efficiency as a function of momentum for the entire detector acceptance range. The left shows the efficiency for selecting K^{+}, the center shows the efficiency for selecting K^{-}, and the right shows the ratio of efficiency in data to that in Monte Carlo.

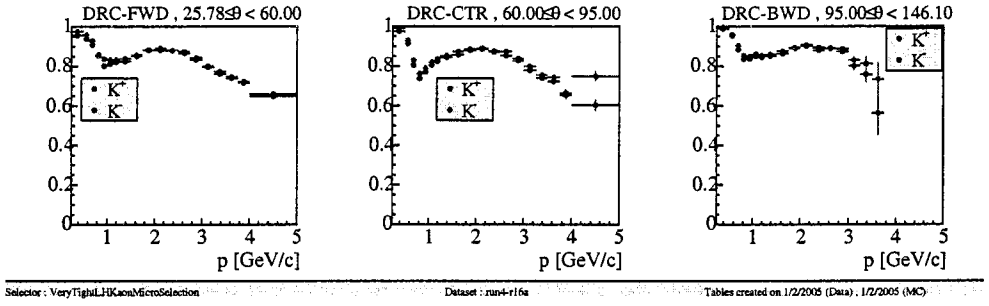

Figure A.8: Efficiencies for selecting $K^{\pm}$s using the `KLHVeryTight` list in data. The histograms show the efficiency for K^{-} and K^{+} as a function of momentum for the forward section of the detector (left), the center section (center), and the backward section (right)

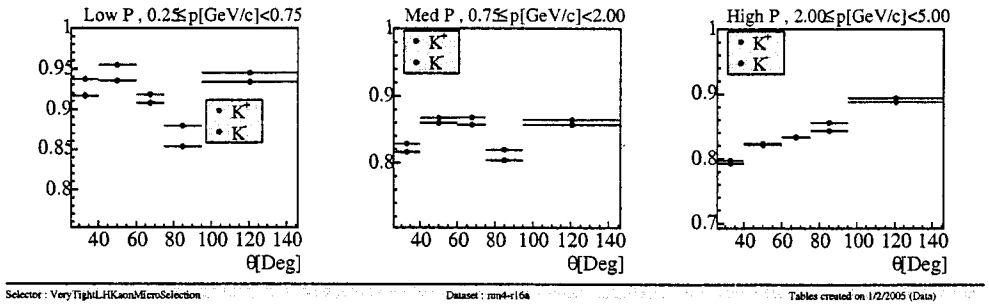

Figure A.9: Efficiencies for selecting $K^{\pm}$s using the `KLHVeryTight` list in data. The histograms show the efficiency for K^- and K^+ as a function of polar angle for the low-momentum tracks (left), medium-momentum tracks (center), and high-momentum tracks (right)

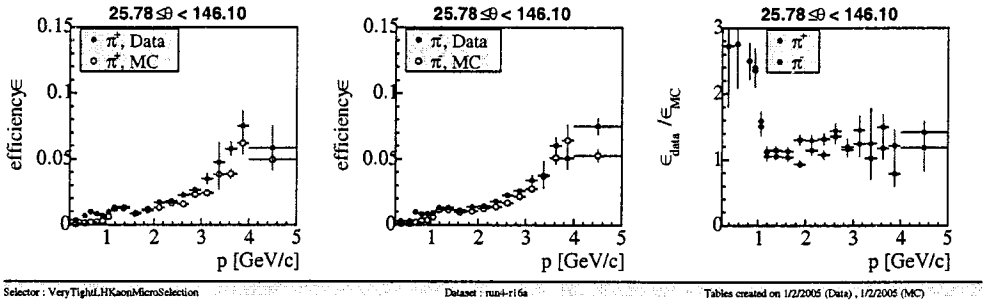

Figure A.10: Efficiencies for selecting $\pi^{\pm}$s using the `KLHVeryTight` list in Monte Carlo and data. The histograms show the efficiency as a function of momentum for the entire detector acceptance range. The left shows the efficiency for selecting π^+, the center shows the efficiency for selecting π^-, and the right shows the ratio of efficiency in data to that in Monte Carlo.

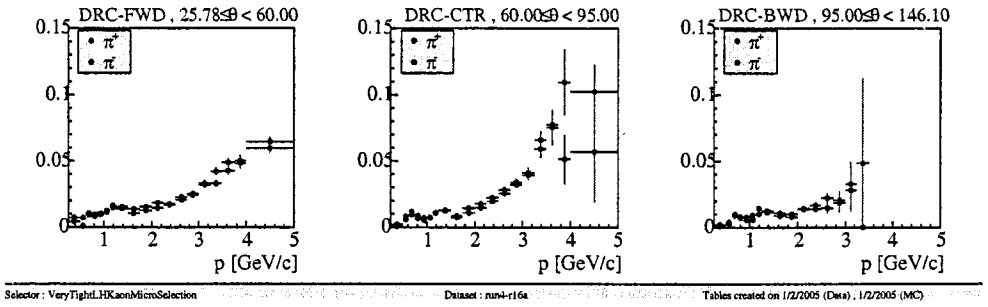

Figure A.11: Efficiencies for selecting $\pi^{\pm}$s using the `KLHVeryTight` list in data. The histograms show the efficiency for π^- and π^+ as a function of momentum for the forward section of the detector (left), the center section (center), and the backward section (right)

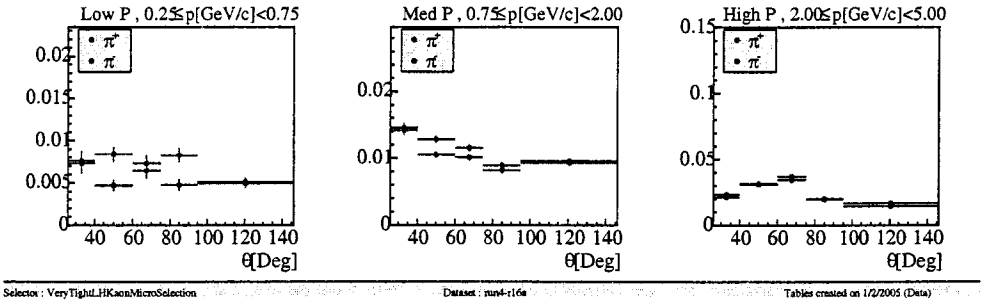

Figure A.12: Efficiencies for selecting $\pi^{\pm}$s using the `KLHVeryTight` list in data. The histograms show the efficiency for π^- and π^+ as a function of polar angle for the low-momentum tracks (left), medium-momentum tracks (center), and high-momentum tracks (right)

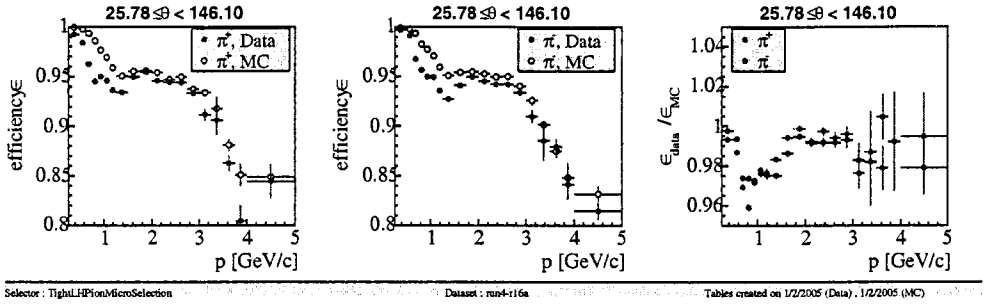

Figure A.13: Efficiencies for selecting $\pi^{\pm}$s using the `piLHTight` list in Monte Carlo and data. The histograms show the efficiency as a function of momentum for the entire detector acceptance range. The left shows the efficiency for selecting π^{+}, the center shows the efficiency for selecting π^{-}, and the right shows the ratio of efficiency in data to that in Monte Carlo.

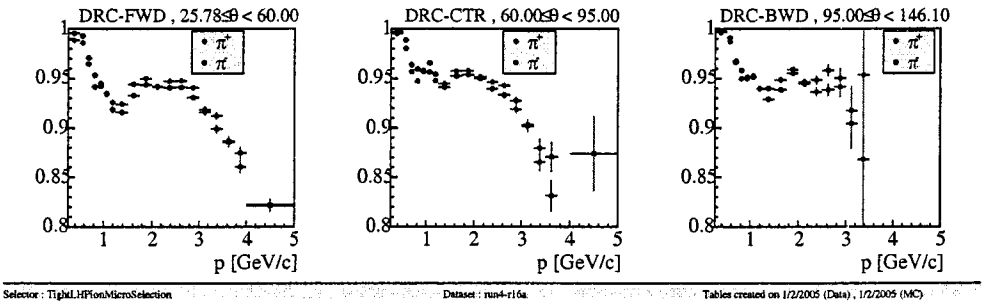

Figure A.14: Efficiencies for selecting $\pi^{\pm}$s using the `piLHTight` list in data. The histograms show the efficiency for π^{-} and π^{+} as a function of momentum for the forward section of the detector (left), the center section (center), and the backward section (right)

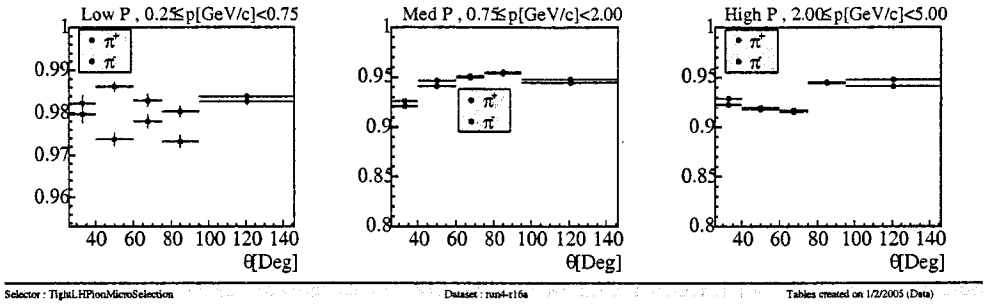

Figure A.15: Efficiencies for selecting $\pi^{\pm}$s using the `piLHTight` list in data. The histograms show the efficiency for π^- and π^+ as a function of polar angle for the low-momentum tracks (left), medium-momentum tracks (center), and high-momentum tracks (right)

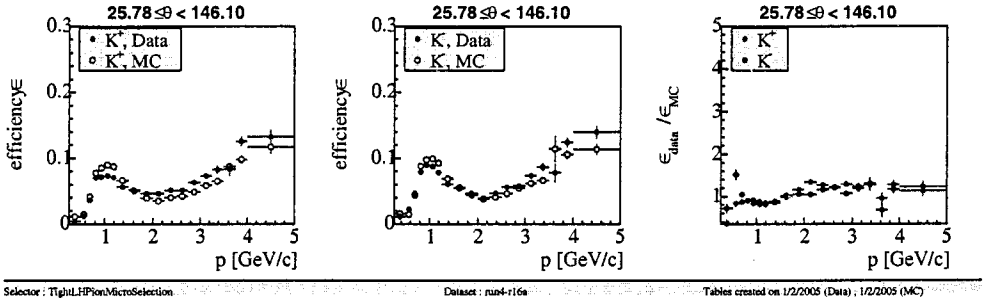

Figure A.16: Efficiencies for selecting $K^{\pm}$s using the `piLHTight` list in Monte Carlo and data. The histograms show the efficiency as a function of momentum for the entire detector acceptance range. The left shows the efficiency for selecting K^+, the center shows the efficiency for selecting K^-, and the right shows the ratio of efficiency in data to that in Monte Carlo.

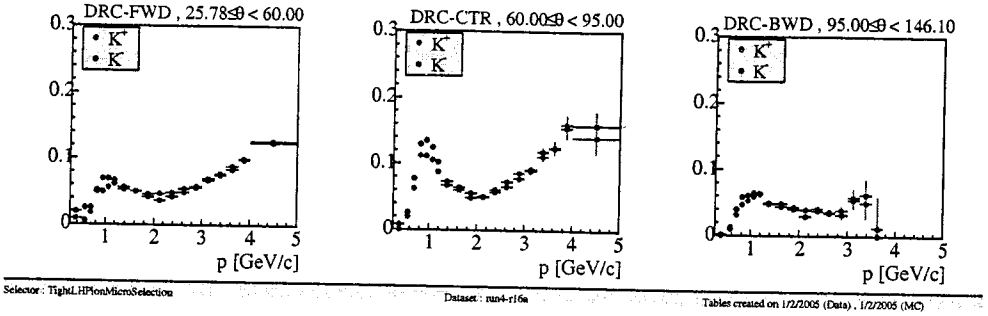

Figure A.17: Efficiencies for selecting $K^{\pm}$s using the `piLHTight` list in data. The histograms show the efficiency for K^- and K^+ as a function of momentum for the forward section of the detector (left), the center section (center), and the backward section (right)

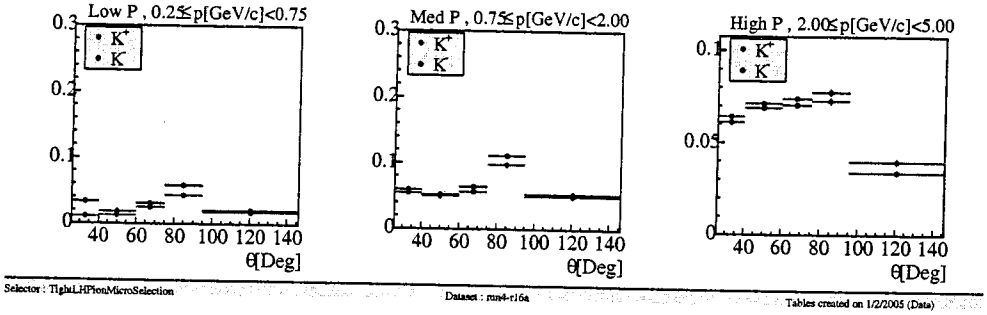

Figure A.18: Efficiencies for selecting $K^{\pm}$s using the `piLHTight` list in data. The histograms show the efficiency for K^- and K^+ as a function of polar angle for the low-momentum tracks (left), medium-momentum tracks (center), and high-momentum tracks (right)

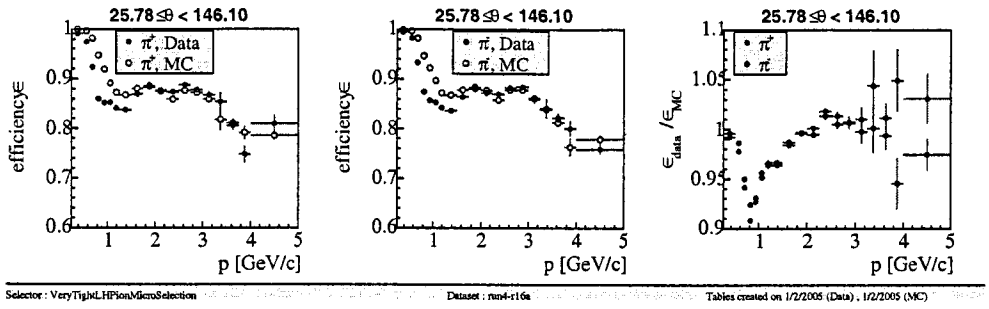

Figure A.19: Efficiencies for selecting $\pi^{\pm}$s using the `piLHVeryTight` list in Monte Carlo and data. The histograms show the efficiency as a function of momentum for the entire detector acceptance range. The left shows the efficiency for selecting π^{+}, the center shows the efficiency for selecting π^{-}, and the right shows the ratio of efficiency in data to that in Monte Carlo.

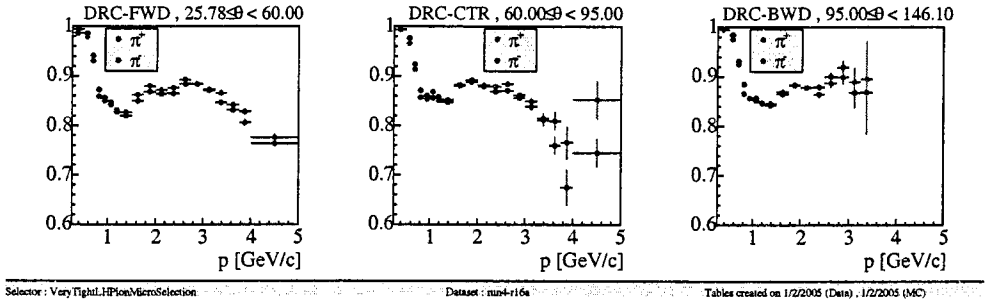

Figure A.20: Efficiencies for selecting $\pi^{\pm}$s using the `piLHVeryTight` list in data. The histograms show the efficiency for π^{-} and π^{+} as a function of momentum for the forward section of the detector (left), the center section (center), and the backward section (right)

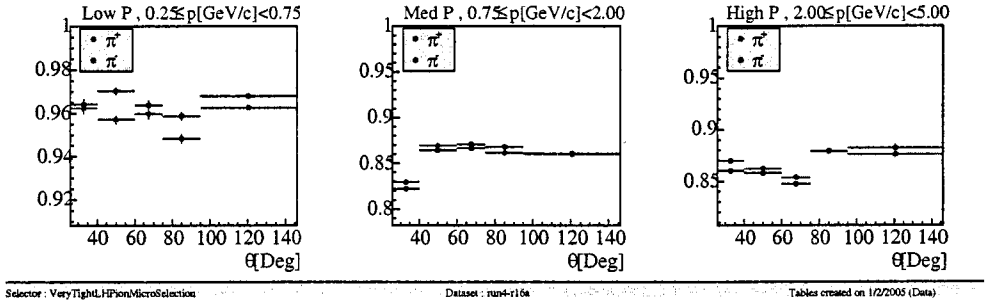

Figure A.21: Efficiencies for selecting $\pi^{\pm}$s using the `piLHVeryTight` list in data. The histograms show the efficiency for π^- and π^+ as a function of polar angle for the low-momentum tracks (left), medium-momentum tracks (center), and high-momentum tracks (right)

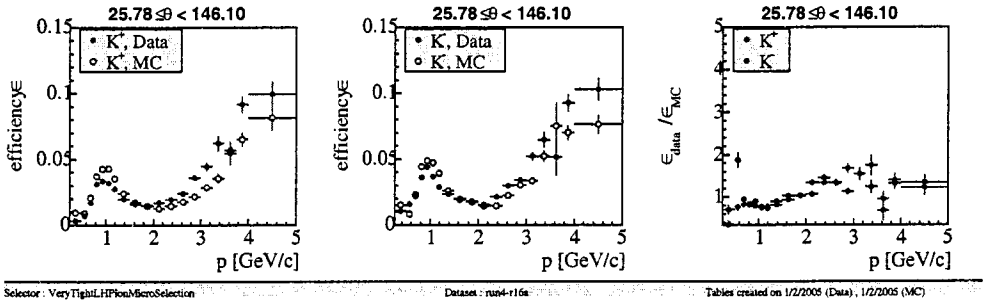

Figure A.22: Efficiencies for selecting $K^{\pm}$s using the `piLHVeryTight` list in Monte Carlo and data. The histograms show the efficiency as a function of momentum for the entire detector acceptance range. The left shows the efficiency for selecting K^+, the center shows the efficiency for selecting K^-, and the right shows the ratio of efficiency in data to that in Monte Carlo.

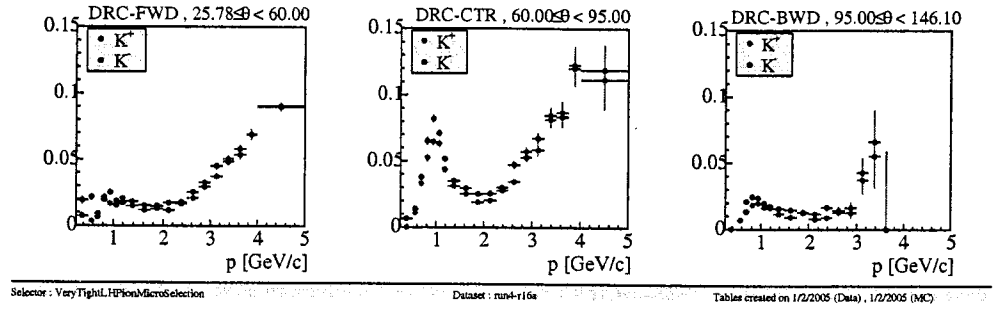

Figure A.23: Efficiencies for selecting $K^{\pm}$s using the `piLHVeryTight` list in data. The histograms show the efficiency for K^- and K^+ as a function of momentum for the forward section of the detector (left), the center section (center), and the backward section (right)

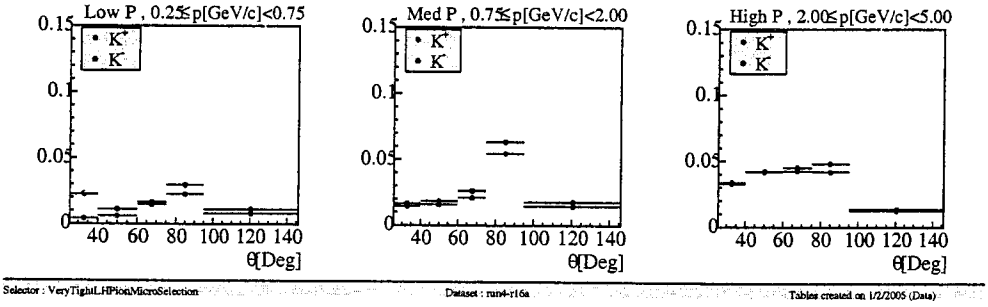

Figure A.24: Efficiencies for selecting $K^{\pm}$s using the `piLHVeryTight` list in data. The histograms show the efficiency for K^- and K^+ as a function of polar angle for the low-momentum tracks (left), medium-momentum tracks (center), and high-momentum tracks (right)

Bibliography

[1] Particle Data Group, S. Eidelman *et al.*, Phys. Lett. **B592**, 1 (2004).

[2] I. I. Y. Bigi and A. I. Sanda, Camb. Monogr. Part. Phys. Nucl. Phys. Cosmol. **9**, 1 (2000).

[3] F. Buccella, M. Lusignoli, G. Miele, A. Pugliese and P. Santorelli, Phys. Rev. **D51**, 3478 (1995), [hep-ph/9411286].

[4] CDF, D. Acosta *et al.*, Phys. Rev. Lett. **94**, 122001 (2005), [hep-ex/0504006].

[5] M. Pivk and F. R. Le Diberder, Nucl. Instrum. Meth. **A555**, 356 (2005), [physics/0402083].

[6] BABAR, B. Aubert *et al.*, Nucl. Instrum. Meth. **A479**, 1 (2002), [hep-ex/0105044].

[7] BABAR, B. Aubert *et al.*, Phys. Rev. Lett. **91**, 121801 (2003), [hep-ex/0306003].